

The effect of the present-day imbalance on schematic and climate forced simulations of the West Antarctic Ice Sheet collapse

Tim van den Akker^{1,2,3}, William H. Lipscomb⁴, Gunter R. Leguy⁴, Willem Jan van de Berg¹, Roderik S.W. van de Wal^{1,5,6}

¹Institute for Marine and Atmospheric Research Utrecht, Utrecht University, Netherlands

²Department of Geological Sciences, Stockholm University, Stockholm, Sweden

³Bolin Centre for Climate Research, Stockholm University, Stockholm, Sweden

⁴Climate and Global Dynamics Laboratory, NSF National Center for Atmospheric Research, Boulder, CO, USA

⁵Department of Physical Geography, Utrecht University, Netherlands

⁶Royal Netherlands Meteorological Institute, De Bilt, Netherlands

Correspondence to: Tim van den Akker (jim.vandenakker@geo.su.se)

Abstract

Recent observations reveal that the West Antarctic Ice Sheet is rapidly thinning, particularly at its two largest outlet glaciers, Pine Island Glacier and Thwaites Glacier, while East Antarctica remains relatively stable. Ice sheet model projections over the next few centuries give a mixed picture, some ice sheet models forced by climate models project mass gain by increased surface mass balance, while most models project moderate to severe mass loss by increasing ice discharge. In this study, we explore the effect of present-day ice thickness change rates on forced future simulations of the Antarctic Ice Sheet using the Community Ice Sheet Model (CISM). We start with a series of schematic, uniform ocean temperature perturbations in the Amundsen Sea Embayment (ASE) to probe the sensitivity of the modelled present-day imbalance to ocean warming. We then apply ocean and atmospheric forcing from seven datasets produced by five Earth System Models (ESMs) from the CMIP5 and CMIP6 ensemble to simulate the Antarctic Ice Sheet from 2015 to 2500. The schematic experiments suggest the presence of an ice-dynamical limit: Thwaites Glacier (TG) does not collapse in these experiments (i.e., with accelerated deglaciation leading to considerable grounded ice mass loss) before ~2100 without more than 2 degrees of ocean warming. Meanwhile, the maximum rate of Global Mean Sea Level rise (GMSLR) from the ASE during the collapse increases linearly with ocean temperature, indicating that while earlier collapse timing shows diminishing returns, the rate of sea-level rise keeps on intensifying with stronger forcing. The relative importance of including the observed present-day mass loss rates decreases for larger (ocean) warming under climate forcing, and decreases over time. For the East Antarctic Ice Sheet on shorter timescales (until 2100), adding the present-day observed mass change rates doubles its global mean sea level rise contribution. On longer timescales (2100–2500), the effect of the present-day observed mass change rates is smaller. Thinning of the West Antarctic Ice Sheet induced by the present-day imbalance is partly compensated by present-day ice sheet thickening of the East Antarctic

Deleted: Lipscomb²

Deleted: Leguy²

Formatted: Superscript

Deleted: ^{3,4}

Formatted: Font color: Auto, English (UK)

Formatted: p1, Space After: 0 pt, Line spacing: 1.5 lines

Deleted: ²Climate

Formatted: Font color: Auto, English (UK)

Formatted: p1, Line spacing: 1.5 lines

Deleted: ³Department

Formatted: Font color: Auto, English (UK)

Formatted: p1, Space After: 0 pt, Line spacing: 1.5 lines

Deleted: ⁴KNMI Royal

Deleted: De

Formatted: Font color: Auto, English (UK)

Formatted: Font color: Auto, English (UK)

Deleted: t

Deleted: uu.nl

Deleted: ,

Deleted: cannot

Deleted: .

Deleted: schematic, sudden and uniform

Deleted: rate

Deleted: to a small degree

47 Ice Sheet over the coming centuries, which persists in our simulations. These deviations are overshadowed by the mass losses
48 induced by the projected ocean warming.

Deleted: Moreover, these

50 1 Introduction

Formatted: Font: Bold

Formatted: Normal

51 The latest IPCC estimate of the Antarctic Ice Sheet (AIS) contribution to global mean sea level (GMSL) rise ranges from 0.03
52 m (SSP1-1.9, low end of the likely range) to 0.34 m (SSP5-8.5, high end of the likely range) in 2100 (Fox-Kemper et al.,
53 2021). This is an assessment based on ice sheet models, which simulate the future behaviour of the AIS. The uncertainty in
54 modelled ice sheet contribution to sea level from the AIS until 2100 is relatively low because the major floating ice shelves
55 keep the grounded ice sheet currently in place (Van De Wal et al., 2022), but increases rapidly after 2100 because non-linear
56 processes could accelerate mass loss significantly (Fox-Kemper et al., 2021; Payne et al., 2021; DeConto et al., 2021). It is
57 argued that the main contributors to Antarctic mass loss uncertainty in the long term (e.g. after 2100) are the choice of ice flow
58 model and the choice of the Earth System Model (ESM) used as ocean and atmospheric forcing (Pattyn and Morlighem, 2020;
59 Aschwanden et al., 2021).

Deleted: behavior

Deleted: Deconto

Deleted: on

60 Both ice flow models and ESMs have grown in number over the past decades. This has increased the capability to quantify the
61 uncertainty related to the choice of the ice sheet model and to the choice of ESM forcing. The Ice Sheet Model Intercomparison
62 for CMIP6 (ISMIP6, Nowicki et al. (2016); (2020)) exemplifies multi-model ensemble simulations of the AIS and state-of-
63 the-art quantification of different sources of uncertainty in sea level rise projections. Seroussi et al. (2023) show that until
64 2100, the choice of ice sheet model (which encompasses all modelling choices, including the momentum balance
65 approximation, resolution, initialization method and parameterizations) is the dominant source of uncertainty of projected
66 GMSL from the AIS, with a growing uncertainty caused by the choice of ESM forcing over time. This study shows large
67 geographic differences: for example, the variance associated with the ice sheet model is large for Thwaites Glacier (TG) and
68 Pine Island Glacier (PIG), which at present-day exhibit the largest ice thinning rates according to recent observations (Smith
69 et al., 2020), and small for the MacAyeal and Whillans glaciers. In a follow-up study, Seroussi et al. (2024) show that the
70 choice of ice flow model remains the largest source of uncertainty until 2300, with ESM forcing as second largest contributor.
71 Among other model differences, a main difference is the method used to simulate the present-day state of the AIS, here referred
72 to as the initialization method.

Deleted: modellers

Deleted: made like

Deleted:

73 To obtain a good model representation of the present-day configuration of the AIS it is necessary to do a model initialization.
74 In an initialization, modellers often include the observed ice thickness and/or the observed ice surface velocities as target
75 variables for the model to match (Winkelmann et al., 2011; Pollard and Deconto, 2012; Greve and Blatter, 2016; Quiquet et
76 al., 2018; Lipscomb et al., 2019; Berends et al., 2021; Berends et al., 2022).. In these methods, the ice sheet model parameters
77 are adjusted by comparing modelled and observed ice surface velocities while either imposing observed ice thickness and/or

Deleted: initialization.

Deleted: adjusts model

87 ice surface velocities (the so-called Data Assimilation method) or by doing a forward run with either historical or present-day
88 forcing (the spin-up method). This process can lead in some cases to nonzero ice thickness change rates, or drift, when the
89 model is run forward in time, even without external climate forcing. All three studies by Rosier et al. (2021), Bett et al. (2023)
90 and Rosier et al. (2024) state that it is impossible to obtain a perfect fit between observed and modelled ice thickness, ice
91 surface velocities, and mass change rates simultaneously because the three datasets are not mutually consistent (Morlighem et
92 al., 2011).

93
94 To get the modelled ice sheet to exhibit a mass change rate, ideally also close to observations, a historical forcing scenario can
95 be used (Reese et al., 2023; Coulon et al., 2024; Klose et al., 2024). Recently, Van Den Akker et al. (2025b) developed a
96 method to incorporate the observed mass change rates in this spin-up initialization, in which the gridded observed mass change
97 rates are subtracted from the mass transport equation. In this way, the resulting modelled ice sheet can start future simulations
98 immediately from the observed imbalance. This circumvents the need for a historical simulation and forcing over the near-
99 present period. Van Den Akker et al. (2025b) show that initialization with the present-day observed mass change rates in two
100 ice-sheet models always leads to an unforced collapse (i.e., without additional ocean or atmospheric warming) of the West
101 Antarctic Ice Sheet (WAIS), starting with Thwaites Glacier (TG) and Pine Island Glacier (PIG). The rapid collapse phase
102 typically begins after a period of 500 - 2000 years of slow retreat. However, that study only showed simulations with a
103 sustained present-day climate; it did not investigate how the present-day imbalance affects simulations that include future
104 climate change (hereafter labelled as 'forcing').

105
106 In this study, we focus on forced simulations of the Antarctic Ice Sheet, first using schematic ocean warming, and secondly
107 ocean temperature and SMB anomalies from five ESMs from the CMIP5 and CMIP6 ensembles following either the SSP1-
108 2.6, SSP5-8.5, RCP1-26 or the RCP 5-85 scenario. The schematic forcing consists of a targeted (e.g. only at TG and PIG)
109 sudden uniform ocean warming up to 2 degrees. The ESM forcing used in this study has also been used as forcing for the
110 ISMIP6 Antarctic Ice Sheet study in Seroussi et al. (2024). These anomalies serve as input to long-term future simulations
111 from 2015 to 2500, to capture the longer-term effects of climate change on the mass of the ice sheet. We use two initializations
112 of the Antarctic ice sheet to start our future simulations, namely with and without the observed mass change rates. Hence, the
113 latter starts from steady-state. With these simulations we investigate the importance for the future evolution of the Antarctic
114 Ice Sheet (AIS) of the current imbalance of the AIS compared to projected future changes in ocean temperature and SMB. For
115 example, do they add up linearly, or does the present-day imbalance influence the forced deglaciation of the WAIS? In section
116 2, we introduce the Community Ice Sheet Model, and we discuss the general initialization procedure and the oceanic and
117 atmospheric ESM forcings used. In section 3, we show the results of the future projections. Section 4 contains the discussion,
118 followed by conclusions in section 5.

119 2 Methods

120

Deleted: with

Deleted: with

Deleted: such a

Deleted: that

Deleted: will

Formatted: Font: Bold

2.1 Community Ice Sheet Model (CISM)

The Community Ice Sheet Model (CISM, (Lipscomb et al., 2019; Lipscomb et al., 2021)) is a thermo-mechanical higher-order ice sheet model, which is part of the Community Earth System Model version 2 (CESM2 (Danabasoglu et al., 2020)). Earlier applications of CISM to Antarctic Ice Sheet retreat can be found in Lipscomb et al. (2021); Berdahl et al. (2023); Van Den Akker et al. (2025b); Van Den Akker et al. (2025a). The variables and constants used in the text and equations below are listed in Supplementary Tables S1 and S2.

We run CISM with a vertically integrated approximation to the momentum balance, the Depth Integrated Viscosity Approximation (DIVA) (Goldberg, 2011; Lipscomb et al., 2019; Robinson et al., 2022):

$$\frac{\partial}{\partial x} \left(2\eta H \left(2\frac{\partial u}{\partial x} + \frac{\partial v}{\partial y} \right) \right) + \frac{\partial}{\partial y} \left(\eta H \left(\frac{\partial u}{\partial y} + \frac{\partial v}{\partial x} \right) \right) - \tau_{b,x} = \rho_i g H \frac{\partial s}{\partial x} \quad (1)$$

$$\frac{\partial}{\partial x} \left(\eta H \left(\frac{\partial u}{\partial y} + \frac{\partial v}{\partial x} \right) \right) + \frac{\partial}{\partial y} \left(2\eta H \left(2\frac{\partial v}{\partial y} + \frac{\partial u}{\partial x} \right) \right) - \tau_{b,y} = \rho_i g H \frac{\partial s}{\partial y} \quad (2)$$

in which η is the depth-averaged viscosity, H the ice thickness, u and v respectively the depth-averaged ice velocities in the x- and y-direction, ρ_i the density of glacial ice and s the surface height above sea level. Basal friction, which appears as $\tau_{b,x}$ and $\tau_{b,y}$ in Eqs. 1 and 2, can be parameterized in several ways. In this study we use a regularized Coulomb sliding law first suggested by Schoof (2005) and confirmed with laboratory experiments by Zoet and Iverson (2020):

$$\tau_b = \beta u_b = C_c N \left(\frac{u_b}{u_b + u_0} \right)^{\frac{1}{m}} \quad (3)$$

where C_c is a unitless parameter in the range [0,1] controlling the strength of the regularized Coulomb sliding, u_b the ice basal velocities and u_0 and m are free parameters. The effective pressure N is estimated according to Leguy et al. (2014) and Leguy et al. (2021):

$$N = \rho_i g H \left(1 - \frac{H_f}{H} \right)^p \quad (4a)$$

where the flotation thickness H_f is given by

$$H_f = \left(0, -\frac{\rho_w}{\rho_i} b \right) \quad (4b)$$

with ρ_i for the density of glacial ice, ρ_w the density of ocean water, g the gravitational acceleration and b the height of the bedrock. In Eq. 4a, p (a parameter in the range [0,1]) controls the decrease in effective pressure of ice resting on bedrock below sea level. Setting $p = 1$ implies that, at the modelled grounding lines, the overburden pressure at the ice base is completely

Formatted: Font: Bold

Formatted: Normal

Deleted: = ρ_i

Deleted: .1

Deleted: = ρ_i

Deleted: 1.

Deleted: in

Deleted: 1.1 and 1.2, can be parameterized in several ways. In this study we use the regularized Coulomb sliding law first suggested by Joughin et al. (2019)

Deleted: 1.

Deleted: (2021), assuming full ocean connectivity and based on the height above flotation of the grounded ice. This implies that the scheme proposed by Leguy et al. (2014) accounts for basal water pressure (which reduces N) only near grounding lines and not in other parts of the ice sheet; thus the effective pressure equals ice overburden for most of the ice sheet. The effective pressure is then calculated by:

Deleted: (1.

Deleted: (1.

170 [balanced by the ocean pressure, and \$N\$ approaches zero. In this study we use \$p=I\$, assuming full connectivity of the subglacial](#)
 171 [hydrological network with the ocean. This scheme, proposed by Leguy et al. \(2014\), accounts for basal water pressure \(which](#)
 172 [reduces \$N\$ \) only near grounding lines and not in other parts of the ice sheet; thus the effective pressure equals ice overburden](#)
 173 [for most of the ice sheet.](#)

174
 175 Since C_c is poorly constrained by theoretical considerations and observations, we use it as a spatially variable tuning parameter.
 176 We tune the logarithm of C_c using a nudging method, [i.e. a 10 kyr simulation with present-day forcing in which the modelled](#)
 177 [ice sheet is allowed to evolve freely while slowly changing \$C_c\$ based on an observational thickness target](#) (Lipscomb et al.,
 178 2021; Pollard and Deconto, 2012):

$$\frac{dC_l}{dt} = -\left(\frac{H - H_{obs}}{H_0\tau}\right) - \frac{2}{H_0} \frac{dH}{dt} - \frac{r}{\tau}(C_l - C_{lr}) + \frac{L^2}{\tau} \Delta C_l \quad (5a)$$

$$C_l = \log(C_c) \quad (5b)$$

181 In 1.5a, H_0 , τ , r and L are scaling constants, used to adjust the relative weights of the different terms. Increasing/decreasing
 182 H_0 makes the optimization less/more sensitive to ice thickness errors; increasing/decreasing τ makes the changes in C_l per
 183 timestep smaller/larger, increasing/decreasing r draws C_l more/less to the relaxation target C_{lr} ; and increasing/decreasing L
 184 results in a smoother/spikier 2D pattern of optimized C_l . Their values were tested and chosen to represent AIS thickness and
 185 surface velocities well, with minimal drift. Table S2 shows their values.

186
 187 The logarithmic relaxation target C_{lr} is a 2D field that penalizes very high and low values of C_c . It is based on elevation, with
 188 lower values at low elevation where soft marine sediments are likely more prevalent, following Winkelmann et al. (2011). We
 189 chose targets of 0.1 for bedrock below -700 m asl and 0.4 for 700 m asl, with linear interpolation in between, based on
 190 Aschwanden et al. (2013). The motivation for this is that lower elevations deglciate earlier and therefore have more softer
 191 marine till relative to higher elevated bedrock, since they likely were deglciated more in the past compared to regions with
 192 higher bedrock. The parameterization and associated values used to represent marine sediments in Aschwanden et al. (2013),
 193 which rely solely on bedrock elevation, are challenged by the more recent findings of Li et al. (2022), who show that the
 194 likelihood of marine sediment does not directly correlate with bedrock height. Incorporating the likelihood map of Li et al.
 195 (2022) into CISM and analysing the influence of marine sediments on marine-based ice sheets is beyond the scope of this
 196 study, but represents a promising direction for future work.

Deleted: 1.

Deleted: 1.

Deleted: H0

Formatted: Font: Italic

Formatted: Font: Italic

Deleted: H0

Deleted: Cl

Deleted: Cl

Deleted: Clr,

Formatted: Font: Italic

Formatted: Font: Italic

Deleted: Cl.

Deleted:

The last term on the RHS of Eq. (5a) is new compared to Lipscomb et al. (2021), Van Den Akker et al. (2025a) and Van Den Akker et al. (2025b) and is introduced to smooth the pattern of optimized C_c by suppressing large spatial gradients. Smoothing also reduces the model drift as a local grounding line position can no longer be pinned by one grid box with high basal friction.

Basal melt rates (BMR) are calculated using a quadratic relation with a sub-shelf thermal forcing ν during the initialization and the forced simulations:

$$BMR = \gamma_0 \left(\frac{\rho_w c_{pw}}{\rho_i L_f} \right)^2 ([TF_{base} + \delta T, 0])^2 \quad (6)$$

in which the baseline thermal forcing, TF_{base} , is the difference between the melting point and the ocean temperature at the base of the modelled ice shelf, and δT a local correction temperature. The thermal forcing is derived from a climatology based on Southern Ocean observations of the past few decades (Jourdain et al., 2020). This basal melt parameterization was developed and tested by Jourdain et al. (2020) and Favier et al. (2019) with the purpose of modelling present-day Antarctic basal melt rates. The quadratic relationship between thermal forcing and basal melt rates reflects a positive feedback. As the ice shelf melts, freshwater is added to the cavity, which is more buoyant than the saltier ocean water. This causes the sub-shelf meltwater plume to rise faster, and through erosion and upwelling of new warm ocean water, the basal melt rates will increase. Eq. (6) parameterizes this feedback to a reasonable approximation for present-day basal melt rates, but it is unknown how well it simulates basal melt rates for several degrees of (future) ocean warming.

The basal melt rates are tuned through the local correction temperature δT such that the floating ice thickness matches as closely as possible the thickness observations of Morlighem et al. (2020) following a similar procedure as for friction (Eq. 5):

$$\frac{d(\delta T)}{dt} = T_s \left[\left(\frac{H - H_{obs}}{H_0 \tau} \right) + \frac{2}{H_0} \frac{dH}{dt} \right] + \frac{(T_r - \delta T)}{\tau} + \frac{L^2}{\tau} \Delta \delta T, \quad (7)$$

in which T_s is the temperature scale of the nudging method (0.5 K in this study). This tuning increases (decreases) the local correction temperature δT in grid cells where the modelled ice shelf is too thick (thin), increasing (decreasing) the basal melt rates. The tuning includes a relaxation target T_r , being 0, to penalize large deviations from the dataset of Jourdain et al. (2020). The melt sensitivity γ_0 is chosen to be 3.0×10^4 m/yr, which was used in Lipscomb et al. (2021); Van Den Akker et al. (2025b); Van Den Akker et al. (2025a) to obtain basal melt rates in agreement with observations and a shelf average δT close to zero in the Amundsen Sea Embayment, where currently the largest ice shelf melt rates are observed (Adusumilli et al., 2020). The last term is added, as for the C_c optimization in Eq. (5), to suppress large spatial variations in the optimized ocean temperature perturbation field, as large differences of several degrees between adjacent grid cells are physically implausible.

Deleted: 1.

Deleted: dataset consisting of all observations over the past decades com...

Deleted: bined with the climatology made by Jourdain et al. (2020)...

Deleted: 1.

Deleted: 1.

Deleted: 1.

Deleted: 1.

Deleted: to, just

Deleted: 1.

Deleted: surpress

Deleted: spatial gradients

Deleted: is

To prevent abrupt jumps in [modelled](#) quantities at the grounding line (such as basal friction and basal melt), we use a grounding line parameterization from Leguy et al. (2021):

$$f_{float} = -b - \frac{\rho_i}{\rho_w} H \quad (8)$$

When f_{float} is positive it is equal to the distance between the ice shelf base and the ocean floor and hence, the ice is floating. When f_{float} is negative, it can be interpreted as the ice thickness change needed for the ice column to become floating. The variable f_{float} is used to compute the floating fraction as a percentage of grid cell area by bilinearly interpolating its value from cell vertices to the cell areas scaled to the cavity thickness (Leguy et al. (2021)). The grounded and floating fraction of a cell are then used to scale basal friction and basal melting. For the basal melting, this is referred to as the Partial Melt Parameterization (PMP, see Leguy et al. (2021)).

Schematic tests by Seroussi and Morlighem (2018) showed that applying basal melt in proportion to the floating area fraction can lead to an overestimation of grounding line retreat rates; they therefore discouraged the use of PMPs. However, Leguy et al. (2021) conducted similar schematic tests with CISM and found that using a PMP reduced CISM's sensitivity to grid resolution more than the No-Melt Parameterization (NMP) recommended by Seroussi and Morlighem. In more realistic AIS applications of CISM, Lipscomb et al. (2021) found that the PMP produced a moderate sensitivity of grounding line migration rates to grid resolution, lower than the sensitivities to basal melt rate and basal friction parameterizations. These results suggest that the optimal GLP is model-dependent and that for CISM, 4-km grid resolution using a PMP is sufficient for [modelling](#) continental-scale ice sheets on multi-century timescales.

We run CISM on a uniform 4 km grid, justified below, using the grounding line parameterization from Leguy et al. (2021) which scales the basal sliding and melt rate proportionally to its grounded and floating area fraction respectively, [in elements that contain the modelled grounding line](#). Doing so, Leguy et al. (2021) showed that this resolution is adequate to capture grounding line dynamics using CISM and idealized marine ice sheet experiments, Lipscomb et al. (2021) showed that this resolution in combination with the scaling reduces the model result's grid resolution dependency when modelling the AIS.

There are several calving laws in the literature e.g. Yu et al. (2019); Wilner et al. (2023); Greene et al. (2022) and specifically for Greenland (Choi et al., 2018). However, there is no agreed-upon best approach to Antarctic calving (Levermann et al., 2012), and most calving laws struggle to reproduce the observed calving front at multiple locations simultaneously without adjusting local parameters (Amaral et al., 2020). We therefore choose to apply a simple no-advance calving scheme, preventing the calving front from advancing beyond the observed present-day location. The ice shelf front can retreat only through ice shelf thinning. This implies that the ice shelf front can only retreat when the basal melt rates increase greatly and become sufficiently high to remove floating ice upstream of the present-day calving front. In practice, this means that the calving front will only retreat when the basal melt rates are increased greatly, and for present-day conditions, this means that the

Deleted: modeled

Deleted: 1.

Deleted:),

Deleted:).

Deleted: the

Deleted: modeling

Formatted: English (UK)

Deleted: .

289 calving front position is fixed at its observed location. This is a conservative approach, ignoring the possibility of calving-front
 290 retreat through shelf thinning or of shelf collapse by hydrofracturing. The implementation of a more physically-based calving
 291 law in CISM is the topic of ongoing research.

292 2.2 Initializations

293 We perform initializations with or without incorporating the observed present-day mass change rates, hence leading to a
 294 transient and equilibrium initial state, respectively. For the equilibrium initialization, C_c and δT are tuned using Eqs. (5) and
 295 (7) until the modelled ice sheet is in equilibrium, thus $\partial H / \partial t = 0$, given by

$$\frac{\partial H}{\partial t} = -\nabla \cdot (\mathbf{u}H) + B \quad (9)$$

297 In Eq. (9), \mathbf{u} is the vertical mean velocity, and B the sum of the basal and SMBs. For the transient initialization, C_c and δT are
 298 tuned using mass conservation complemented by the present-day observed mass change rates as was done by Van Den Akker
 299 et al. (2025b), using

$$\frac{\partial H}{\partial t} = -\nabla \cdot (\mathbf{u}H) + B - \left. \frac{\partial H}{\partial t} \right|_{obs} \quad (10)$$

301 in which the last term, the pseudo-flux, is the observed mass change from Smith et al. (2020). By subtracting this observed
 302 mass change, mass is added during the initialization where thinning is observed. After the initialization and for normal forward
 303 simulations, this pseudo-flux is removed, so that model simulations start with an imbalance and a thinning rate closely
 304 matching the observed thinning rates. Both initializations are run for 10 kyr, which proved to be long enough to reach a
 305 (thermal) equilibrium. We evaluate both initializations by comparing to observations of ice thickness (Morlighem et al., 2020),
 306 ice surface velocities (Rignot et al., 2011), total basal melt fluxes (Adusumilli et al., 2020; Rignot et al., 2013) and by evaluating
 307 their model drift. We test the drift by running forward for 1000 years (i.e., to the year 3015) without additional forcing with
 308 respect to present-day conditions, with the optimized parameters (e.g. δT and C_c in Eqs. (5) and (7)) kept constant, and
 309 continuing to add the observed mass changes for the transiently initiated model state as described by Eq. (10). This is a time
 310 scale longer than our period of interest, which runs only to 2500, thus for 485 years. The resulting drift, shown in Figures S1
 311 and S2, results in a WAIS change in IVAF over 1000 years of 0.5% for the transient initialization and approximately 0% for
 312 the equilibrium initialization. For the whole AIS, the model drift in the transient initialization is 0.05% of the IVAF and -
 313 0.05% for the equilibrium initialization. These results ensure that we can attribute any major changes in ice sheet mass to the
 314 applied forcing and not to model drift. Figure S3 shows the evolution of the average temperature during the initialization: it
 315 flattens out at 10 kyr, indicating that the ice sheet has reached thermal equilibrium.

316 2.3 Idealized schematic warming scenarios

318

Deleted: 1.

Deleted: 1.

Deleted: $(\mathbf{u}H)\mathbf{u}H(\mathbf{u}H)$

Deleted: 1.

Deleted: 1.8

Deleted: (

Deleted: 1.

Deleted: 1.

Deleted: 1.

Deleted:)

Deleted: with

Deleted: adding

Deleted: 1.

Deleted: Transient

333 To assess how sensitive the simulations starting from the transient initialization are to imposed ocean warming, and to compare
334 this with the sensitivity of simulations starting from the equilibrium initialization, we conduct a set of idealized experiments
335 in which ocean temperatures in the ASE region are systematically increased after initialization.

337 2.4 ESM₂ forced future projections

338 We first test the sensitivity of the two initializations to schematic ocean warming by conducting 11 idealized experiments with
339 sudden and sustained warming, only in the ASE region shown in Figure S3. We raise the ocean temperature, which appears as
340 the sum $TF_{base} + \delta T$ in Eq. (6), from 0 to 2 K with steps of 0.2 K. Each experiment is run for 1000 years to allow for a possible
341 WAIS collapse.

342
343 We then perform two sets (i.e. starting from the transient and starting from the equilibrium initialization) of simulations for
344 each of the seven forcing datasets produced by the five different ESMs, introduced in the next section. We timestamp the end
345 of our initialization at 2015 based on the observational datasets used to calibrate the model (Smith et al., 2020; Morlighem et
346 al., 2020; Rignot et al., 2011). We then run CISM forward for 485 years to 2500. The seven forcing datasets from five different
347 ESMs span the period 1995–2100, with four ESMs continuing until 2300 and one where the input forcing to the ESM was
348 repeated from the late 21st century onwards. For the last 200 years of the simulations, we fix the thermal forcing and SMB
349 anomalies at the last datapoint year (2300). We consider the whole continent in our analysis, but focus on areas with large
350 changes and potentially large sea level contributions, like the Amundsen Sea Embayment, the Filchner-Ronne basin, and the
351 Ross basin. Those areas are shown in Figure S3.

352
353 We use the same set of ocean and SMB forcings as Seroussi et al. (2024). These forcings stem from seven ESM simulations
354 from the CMIP5 and CMIP6 ensemble. Two models from the CMIP5 ensemble were selected by Barthel et al. (2020): the
355 Community Climate Model (CCSM4) and the Hadley Centre Global Environment Model (HadGEM2-ES), with respective
356 Equilibrium Climate Sensitivities (ECS) of 2.9 and 4.6 K (Meehl et al., 2020). Additionally, two CMIP6 participating models
357 are used: the Community Earth System Model (CESM2) and the UK Earth System Model (UKESM), with ECS of respectively
358 5.2 and 5.3 K (Meehl et al., 2020). The Norwegian Earth System Model (NorESM, with an ECS of 2.5 K as reported by Meehl
359 et al. (2020)) was used as a reference run in the ISMIP6 ensemble and will be used in this study as well. The models
360 HADGEM2-ES, CESM2 and UKESM have a climate sensitivity to doubling of CO₂ concentrations at the upper end of the
361 90% confidence interval in the IPCC-AR6 report (Meehl et al., 2020). More information on the selection of these ESM forcings
362 can be found in Barthel et al. (2020) and Seroussi et al. (2024).

Deleted: Each experiment is then run for 1000 years to allow for a possible WAIS collapse. Ocean temperatures are incremented from 0 K to 2 K in 0.2 K steps, yielding ten simulations for each initialization...

Deleted:

Deleted: Future

Deleted: and sudden

Deleted: temperatures in these schematic tests

Deleted: 1.

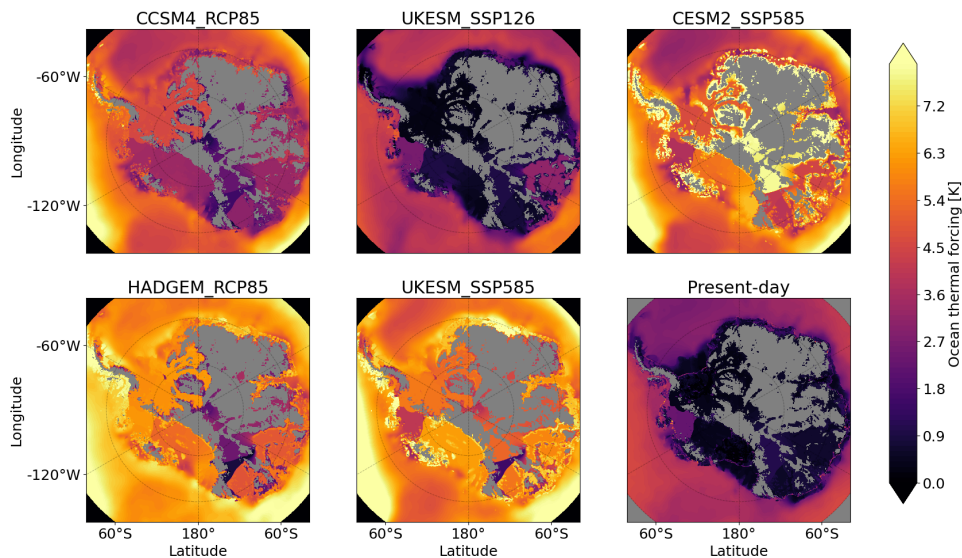
Deleted: being

Deleted: .

Deleted:

Deleted: The ocean and SMB

Deleted: ,



379

Figure 1. Thermal forcing ($TF_{base} + \delta T$ in Eq. (1.6)) from the five ESMs used. Thermal forcing averages for the year 2300 (except the present-day) are shown for a depth of -500 metres. Cells with bedrock above sea level are shown in grey. The simulations from NorESM run until 2100 and are shown in Figure S

383

The ocean forcings from the ESMs are applied similar to the thermal forcing TF_{base} in Eq. (6). For this set of simulations, cavity-resolving ocean models were not available among the CMIP5 and CMIP6 ensembles. Therefore, the ocean thermal forcing from the ESMs is interpolated into the ice shelf cavities following Jourdain et al. (2020). First, a marine connection mask is generated, marking cells with subzero topographic paths to the open ocean. Next, empty cells adjacent to filled ones and connected to the ocean are identified. These cells are then filled with the average of neighboring filled values. Any empty cells below the new fill may remain if the local bedrock is deeper than in adjacent columns. In those cases, the thermal forcing is linearly extrapolated using a depth-dependent freezing point correction with a temperature coefficient of $7.64 \times 10^{-4} \text{ K m}^{-1}$ from Beckmann and Goosse (2003). The last year (2300) of all 7 oceanic forcings, including the extrapolation below present-day grounded ice, relative to TF_{base} , are shown in Figure 1.

393

The computed ocean thermal forcing dataset has 30 layers with a vertical resolution of 60 metres and extends down to 1770 m below sea level. The thermal forcing at the ice-shelf base is linearly interpolated between vertically adjacent ocean layers. If

395

Deleted: 1.

Deleted:

Deleted: by

Deleted: , following Jourdain et al. (2020).

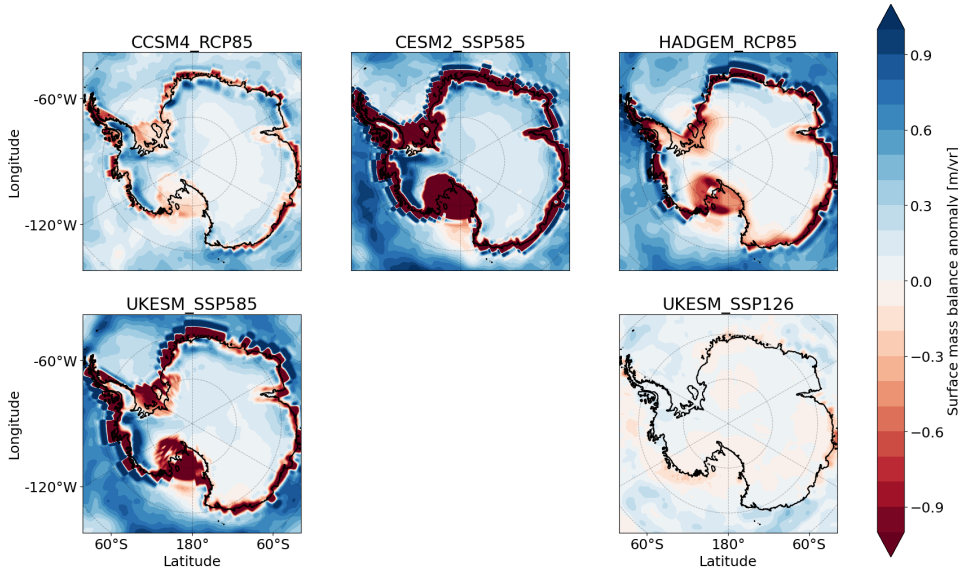
Deleted: The

401 the ice lies below the lowest ocean layer, which can occur in deep troughs beneath the Filchner-Ronne and Amery shelves, the
402 thermal forcing is extrapolated from the lowest layer using the depth-dependent freezing point temperature coefficient from
403 Beckmann and Goosse (2003).

404

405 Figure 2 shows the SMB anomalies of seven simulations of the five ESMs. Large differences in magnitude are visible, with
406 NorESM_RCP26 and NorESM_RCP85 having hardly any change in SMB compared to present day. On the other hand,
407 CESM2_SSP585 and UKESM_SSP585 show large areas where the SMB decreases considerably due to surface melt. For
408 many of these areas the local SMB becomes net negative, which occurs at present in only a few locations (Mottram et al.,
409 2021; Van Wessem et al., 2018). The simulations that show considerable SMB reduction by surface melt over the ice shelves
410 (CCSM4_RCP85, CESM2_SSP585, HADGEM_RCP85 and UKESM_SSP585) also project an increasing SMB for the WAIS
411 ice divide and in Dronning Maud Land. The latter location currently shows thickening as well (Smith et al., 2020).

412



413

414

415 **Figure 2. Surface mass balance (SMB) anomalies simulated by the five ESMs.** The last year of the original datasets, which is 2300 for
416 all simulations except the NorESM simulations, which end in 2100) is shown. Anomalies are added directly to the modelled present-day

Deleted: does occur

Deleted: at very

Deleted: only

Deleted: in the course of time

421 SMB from RACMO (Van Wessem et al., 2018) annually in the continuation simulations. The observed grounding line position is shown in
422 black.

423 Four of the ESMs (CESM4, HadGEN2-ES, CESM2 and UKESM) were run forward from the historical period until 2300,
424 with high emissions continuing long after 2100 in the high-emission scenarios (RCP85 and SSP5-8.5). For these models, we
425 fix the thermal forcing and SMB anomalies at the 2300 values during the last 200 years of the simulation. NorESM,
426 however, was run only until 2100. After 2100, the NorESM forcing in our simulations is held fixed at late 21st century
427 values. Thus, the NorESM forcing is not directly comparable to the other ESMs after 2100.

428 429 3. Results

430 431 3.1 Initialization evaluation

432 Figures 3 - 5 present the key performance metrics for the equilibrium and transient initializations, namely the difference
433 between observed and modelled ice thickness, surface ice velocities and mass change rates. Supplementary Figures S4 and S5
434 show the spatial patterns of the ice thickness and surface velocity errors with respect to observations, and the optimized
435 quantities for both initializations.

436
437 Overall ice thickness biases are low (Fig 3), especially compared to the velocity errors. In both initializations, we tune towards
438 an observed ice thickness target and not to an ice surface velocity target. The velocity biases are relatively high, but still of the
439 same order of magnitude as many ISMIP6 models (see Seroussi et al. (2020)). Including the present-day mass change rates
440 increases the ice thickness and ice velocity RMSE slightly. Furthermore, in areas where large thinning rates are observed, such
441 as PIG and TG, the dynamic imbalance pseudo-flux in Eq. (9) adds considerable mass during the spin-up, which brings the
442 modelled ice fluxes across the grounding line in the transient initialization more in line with observations than in the
443 equilibrium initialization, following Van Den Akker et al. (2025b); Van Den Akker et al. (2025a). Using the same flux gates
444 and calculation as Van Den Akker et al. (2025b), the observed ice fluxes in this study at PIG and TG are $31.1 \text{ km}^2 \text{ yr}^{-1}$ and
445 $26.1 \text{ km}^2 \text{ yr}^{-1}$, respectively. In the equilibrium initialization, those fluxes are $17.0 \text{ km}^2 \text{ yr}^{-1}$ and $17.4 \text{ km}^2 \text{ yr}^{-1}$, hence much lower
446 than observed. Using the present-day mass change rates and the initialization as described in Section 2 results in PIG and TG
447 fluxes of $30.4 \text{ km}^2 \text{ yr}^{-1}$ and $24.5 \text{ km}^2 \text{ yr}^{-1}$, which are in good agreement with observations.

448
449 In areas with observed thickening in the dataset of Smith et al. (2020), such as at the EAIS, the magnitude of the sum of all ice
450 fluxes (including the pseudo flux in Eq. 10) can become similar to or larger than the negative of the SMB. This requires for
451 these locations, for an equilibrated transient ice sheet, a largely reduced ice flux divergence or even ice flux convergence
452 compared to the equilibrated equilibrium ice sheet. Since ice velocities are low at these locations, and therefore the ice flux is

Deleted: presents

Deleted: 1.

Deleted: similarly to as discussed by

Deleted: are

Formatted: Superscript

Formatted: Superscript

Deleted:

Formatted: Superscript

Formatted: Superscript

Formatted: Superscript

Formatted: Superscript

Formatted: Superscript

Formatted: Superscript

Deleted:

Deleted: .

Formatted: Superscript

Formatted: Superscript

Formatted: Superscript

Formatted: Superscript

Deleted: -

Deleted: (1.

Deleted: of

Deleted: magnitude as

464 small, the basal friction cannot always decrease the ice velocity enough to reach a steady state with the correct ice thickness,
465 and hence the ice sheet thins locally until a new equilibrium is reached. Consequently, adding the observed present-day mass
466 change rates in these locations yields a negative modelled ice thickness bias, visible on the EAIS in Figure S2. This increases
467 the RMSE of the modelled ice thickness with respect to observations.

468
469 The ice surface velocity biases are generally low in both initializations, except for the Siple coast glaciers and the Ronne ice
470 shelf. For the Siple Coast, the thickness biases are low, indicating that the friction constant optimization in these spots can
471 nudge the modelled ice thickness close to observations, typically with a low C_c in the ice streams. This apparently leads to an
472 overestimation of the ice surface velocity in these ice streams, which can be counteracted by locally tuning parameters related
473 directly to the ice velocities, like the viscosity or the flow enhancement factor. However, the relative error in these ice streams,
474 where the ice surface velocities exceed 2 km yr^{-1} , is still small.

475
476 The same holds for the Ronne shelf, where the modelled ice surface velocities are too low. The ice thickness error for the
477 Filchner-Ronne shelf in both initializations is low, again indicating that the nudging of δT is capable in reproducing the
478 observed ice thicknesses. However, the nudging of δT does not alter the modelled ice thickness by changing the ice velocities
479 as it does for the friction constant optimization. To obtain a better fit, just as with the glaciers at the Siple Coast, parameters
480 directly related to the ice velocities can be nudged. This decreases the misfit between modelled and observed ice surface
481 velocities as shown by Van Den Akker et al. (2025a), but it also introduces another time-constant but spatially varying
482 parameter with associated uncertainties and the risk of over-tuning.

483
484 Figure 5 shows the binned mass change rates from the observations and both model initializations. The transient
485 initialization reproduces the observed thinning rates almost perfectly. For positive rates, the modeled values begin to diverge
486 from the observations in grounded regions where observed thickening exceeds 0.5 m yr^{-1} , which occurs in less than 0.01% of
487 the modeled grid cells. This discrepancy arises because the model can no longer reduce ice flux by increasing friction; C_a in
488 Eq. 4 has reached its upper limit of 1. The surface mass balance and ice inflow into the cell become insufficient to reproduce
489 the observed mass change. These cases of underestimated ice sheet thickening occur mainly in the interior of the EAIS, a
490 region with little to no dynamic connection to the WAIS.

491
492 For floating grid cells, the model cannot reproduce observed thickening rates because ice accretion is not formally
493 represented in the ISMIP6 basal melt parameterization. This restriction arises from the inability to specify where the positive
494 mass change terms Eq. 9 should be applied, on top or on the bottom of a floating ice column.

Deleted: Regarding

Deleted: at

Deleted: positive

Deleted:

Deleted:

Formatted: Font: Italic

Formatted: Font: Italic, Subscript

Formatted: Font: Italic

Deleted: 1.

Deleted:

Deleted: theWAIS

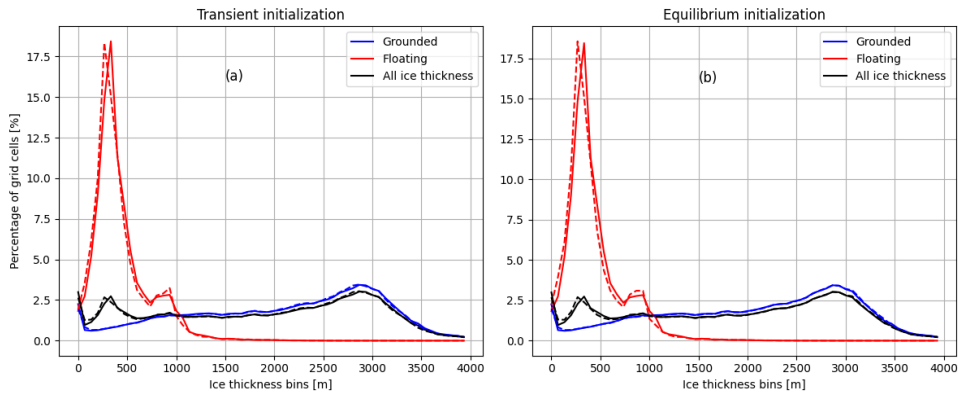
Deleted: 1.

505 The equilibrium simulation presents a different pattern. As expected, it fails to capture the observed present-day mass change
506 rates completely, as it was initialized to be in equilibrium. Consequently, it exhibits minimal model drift, only 0.001% of the
507 modeled grid cells show a drift greater than 0.1 m yr⁻¹.

Deleted: ,

Deleted:

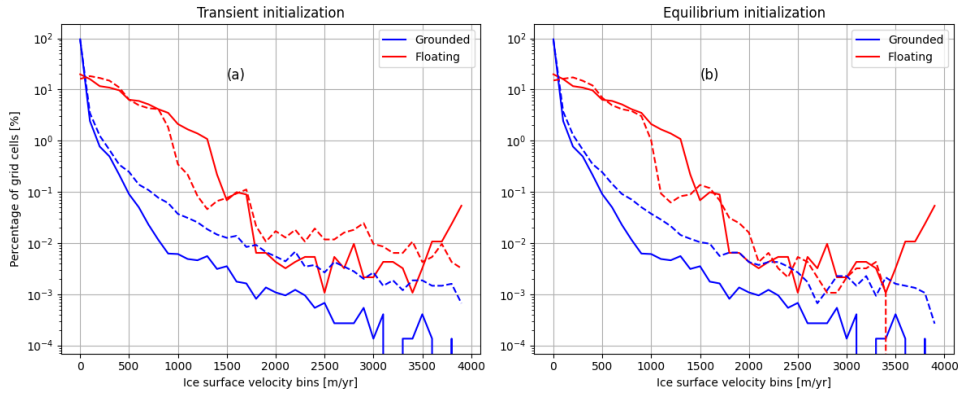
Deleted: ¶



511 **Figure 3. Binned ice thickness (m) for the observed (solid) and modelled ice (dashed lines).** The present-day condition
512 of the transient initialization is shown on the left, the equilibrium simulation on the right. For the transient initialization, the
513 root mean square errors (RMSEs) for floating ice, grounded ice and in total are respectively 44, 31 and 35 meters. For the
514 equilibrium initialization they are respectively 50, 23 and 30 m.

Formatted: Font: Bold

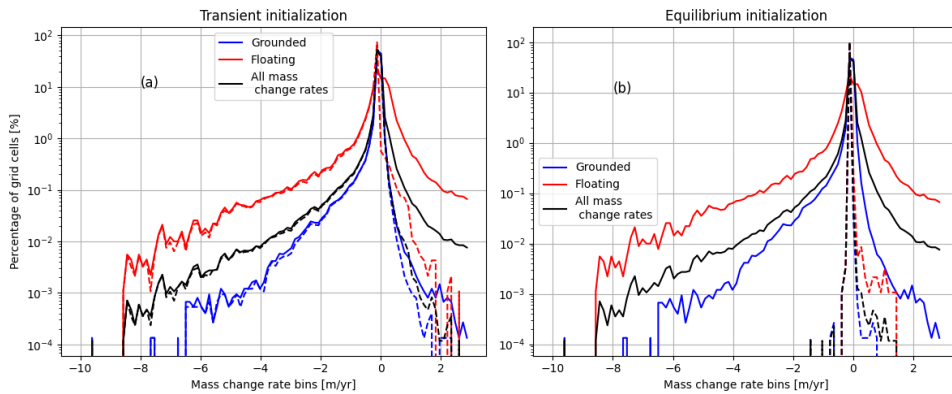
523



524

525 **Figure 4.** Binned ice surface velocities (m yr^{-1}) for the observed (solid) and modelled ice (dashed lines). The present-day
 526 condition of the transient initialization is shown on the left, the equilibrium simulation on the right. For the transient
 527 initialization, the Root Mean Square Errors (RMSEs) for floating ice, grounded ice and in total are respectively 201, 112 and
 528 143 m yr^{-1} . For the equilibrium initialization they are respectively 202, 98 and 130 m yr^{-1} .

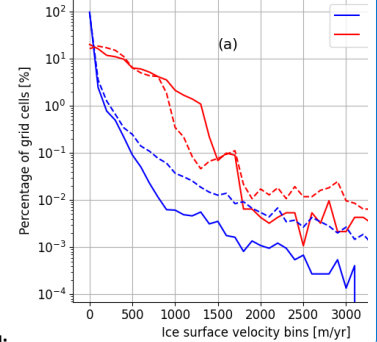
529



530

531 **Figure 5.** Binned mass change rates for the observed ice (solid lines) and the modelled ice (dashed lines). The transient
 532 initialization is shown on the left, and the equilibrium initialization on the right.

533



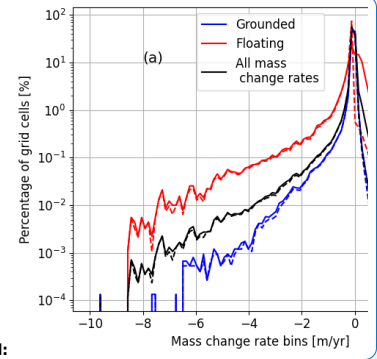
Deleted:

Deleted: 1

Formatted: Font: Bold

Formatted: Superscript

Formatted: Superscript



Deleted:

Formatted: Font: Bold

3.2 Schematically forced Antarctic mass change

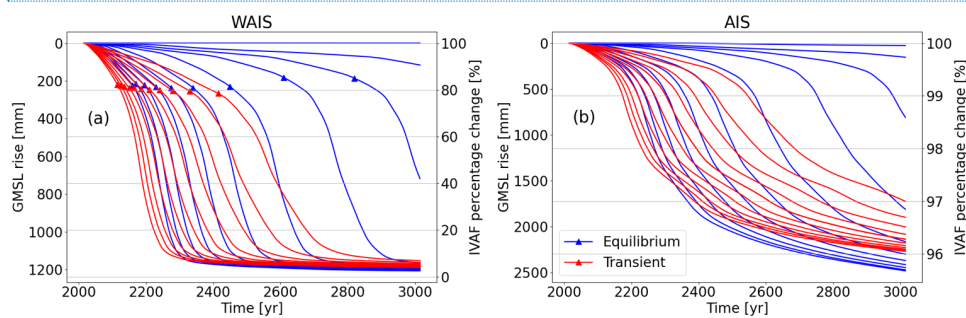


Figure 6. Ice Volume Above Flootation response to sudden, uniform ocean warming of the ASE sector, represented as GMSL rise (left y-axis) and as percentage of what was originally present in the ASE region. (a) integrated mass loss in the ASE, where Thwaites Glacier and Pine Island Glacier are situated. Left y-axis shows the GMSL rise in mm and the Ice Volume Above Flootation (IVAF) in percentage of the initial value. (b) The same for the whole AIS. Red lines indicate simulations starting with the observed mass change rates, blue lines indicate simulations starting from an equilibrium. From right to left (later collapse to earlier collapse) the simulations are forced with 0 to 2 K of ocean warming with steps of 0.2 K. Triangles indicate the timestep when the bedrock ridge approximately 50 km inland of the present-day TG grounding line ungrounds, depicted by the line AB in Fig S6.

Figure 6 presents the integrated GMSL rise resulting from the schematic warming experiments, for both the ASE and the entire AIS. Starting from the transient initialization, applying a uniform and abrupt ocean warming to the ASE triggers an earlier onset of collapse with increasing temperatures, with diminishing sensitivity at higher ocean temperatures, but a larger rate of GMSL rise. The impact of ocean warming is larger in simulations initialized without present-day mass change rates. This can be attributed to the optimized parameter δT , which tends to be lower in these runs. As a result, adding 0.2 K of ocean warming leads to a relatively larger increase in effective ocean temperatures compared to simulations that include present-day mass change rates, where δT is typically higher.

Interestingly, the equilibrium simulations (blue lines in Fig. 6) show a greater long-term GMSL contribution from the AIS compared to the transient simulations. The equilibrium runs are more sensitive to ocean warming, which can be partly attributed to a larger relative increase in δT , and to the stabilizing effect of including present-day mass change rates. Specifically, incorporating these rates makes the Kamb Ice Stream (see Fig S6) more stable, as it is currently thickening (Smith et al., 2020). A more stable Kamb ice stream acts as a brake on the retreat of Siple Coast glaciers once the ASE has lost its grounded ice. In this scenario, the retreat of the grounding line and subsequent ice sheet collapse are less able to propagate

Deleted: Schematically

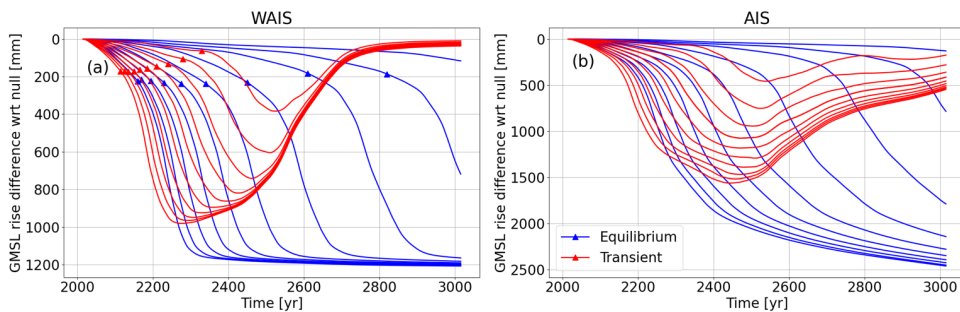
Deleted: Mass

Deleted: 1

567 beyond the ASE, across the WAIS ice divide, and into the Siple Coast region. In contrast, in the equilibrium simulations, where
568 this stabilizing effect is absent, such large-scale collapse can occur more easily.

569

570

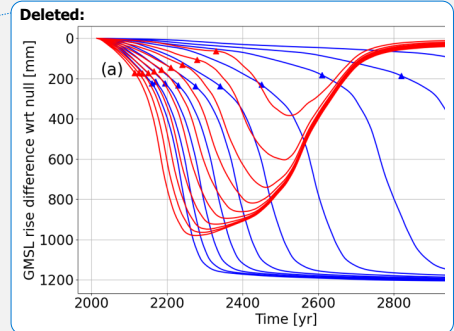


571

572 **Figure 7. All schematic warming scenarios with the control experiment (i.e. 0 ocean warming) subtracted.** For the ASE (a) and the
573 AIS (b) in terms of GMSL rise. Triangles indicate the timestep when the ridge in the bedrock approximately 45 km inland of the present-day
574 TG grounding line ungrounds, depicted by the line AB in Fig S6. Red lines indicate simulations starting with the observed mass change
575 rates; blue lines indicate simulations starting from an equilibrium. From right to left (later collapse to earlier collapse), the simulations are
576 forced with 0.2 to 2 K of ocean warming with steps of 0.2 K. Triangles indicate the timesteps when the line AB in Fig S6 ungrounds
577 completely.

578 To investigate the impact of different initial conditions, we subtracted the results of the no-perturbation simulations (i.e. 0 K
579 of added ocean warming in the ASE) from their corresponding schematically forced simulations (Figure 7). In the case of the
580 equilibrium initialization, the no-perturbation experiment resulted in negligible mass loss, so the mass loss in the forced
581 experiments due to the applied ocean forcing is almost the same as the difference between the forced scenarios and the no-
582 perturbation experiment. In contrast, the unforced transient initialization exhibits a collapse of the WAIS, so Figure 7 shows
583 the deviation from this evolution due to the added ocean forcing.

584 The simulations starting from the transient initialization have a much different response than those starting from the
585 equilibrium initialization. For the first 250 (strong forcing) to 600 (weak forcing) years, the impact of ocean warming is larger
586 for the transient initialisation simulations than for the equilibrium initialization simulations. Positive feedbacks drive the
587 collapse of the WAIS, and these feedbacks are initiated earlier if the simulations start out-of-balance. After the collapse of TG
588 and PIG, the impact of ocean warming ceases in the transient initialization simulations, as the GMSL rise contribution slows
589 down in the final phase of the collapse (Fig. 6b) and the WAIS can only collapse once. This ceasing effect will not occur for



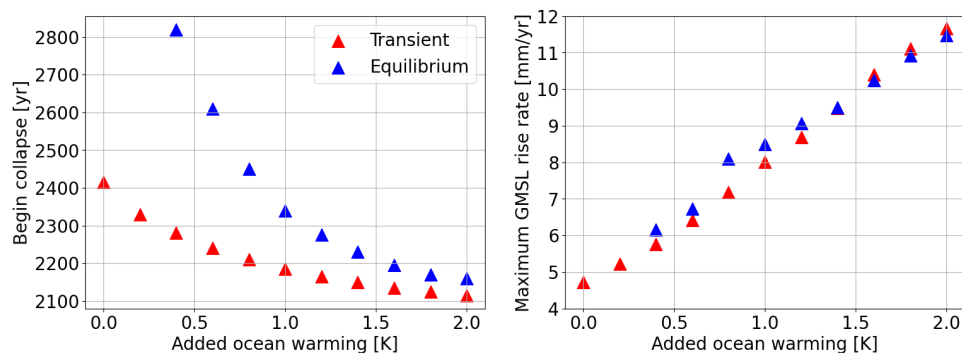
Deleted: subtracted

Deleted: ,

Deleted:)

Deleted: initializations

596 the equilibrium initialization simulations, as the ocean forcing induces all the GSML rise contribution and the collapse of the
597 WAIS, which otherwise would not happen.



598

599 **Figure 8. Impact of ocean warming on the beginning of the collapse and maximum GSML rate.** (left) The beginning of the WAIS
600 collapse defined as the ungrounding of ridge AB in Van Den Akker et al. (2025b) as function of added uniform and sudden ocean warming
601 in the ASE. Blue dots represent simulations. (right) the maximum GSML rise rate modelled in the same simulations, also as function of the
602 added ocean warming.

603

604 In Figure 8, increasing ocean warming is correlated with an earlier onset of TG collapse, which in our simulations consistently
605 acts as the precursor to WAIS collapse. In this study, all collapse events initiate at TG. The onset of collapse is defined as the
606 first timestep at which the bedrock ridge, 50 km upstream the current grounding line (see Figure S6) becomes entirely free of
607 grounded ice. The role of this bedrock ridge is discussed in more detail by Van Den Akker et al. (2025b). The results show
608 that higher ocean temperatures lead to earlier collapse, but with progressively smaller shifts in timing. This suggests the
609 presence of a limit on the onset of collapse: ~~TG cannot collapse before ~2100 without more than 2 degrees of ocean warming.~~
610 Meanwhile, the maximum GSML rise rate during the collapse increases linearly with ocean temperature, indicating that while
611 earlier collapse timing shows diminishing returns, the rate of sea-level rise keeps on intensifying with stronger forcing. The
612 additional sea-level contribution can come not only from PIG and TG, but also from the neighbouring Pope, Smith and Kohler
613 glaciers, which are in the same basin as TG and therefore receive the same ocean warming. Furthermore, simulations starting
614 from an ice sheet in equilibrium have the collapse delayed by multiple centuries compared to the transient initialization
615 simulations. Here, however, warmer ocean waters still bring the collapse onset forward, without approaching a limit. It is
616 noteworthy that the maximum GSML rise rate, if reached, is comparable to transient initialization runs.

617

Deleted: an

Deleted: ,

3.3 Realistically forced future Antarctic mass change

Figure 9 shows the simulated integrated ice sheet mass loss in the Amundsen Sea Embayment (ASE) as well as for the entire Antarctic Ice Sheet. Until 2150, the projected mass loss is largely determined by the initialisation method; hence the current dynamic imbalance sets the short term mass loss of the ASE. After 2150, all simulations project eventual WAIS collapse, in most cases before 2500. Simulations initialized with the transient initialization configuration (solid lines) predict faster ice mass loss and an earlier collapse than those initialized with the equilibrium initialization configuration (dashed lines). This accelerated ice mass loss when using the transient initialization compared to the equilibrium initialization and collapse due to transient initialization occurs 50 to 100 years earlier under low emission scenarios (SSP126 or RCP26) and 25 to 50 years earlier under high-emission scenarios. These findings highlight the impact of the present-day imbalance on WAIS projections and emphasize the need to include those in regional simulations. The influence of this imbalance is more pronounced under cooler scenarios, where future ocean warming and surface melting is less dominant. In warmer scenarios (RCP8.5 and SSP5-85), the strong ocean forcing and net negative SMB diminish the relative impact of model initialization choices. Similar results have been described for glacial isostatic adjustment applications by Van Calcar et al. (2024) who argue that the details of the GIA matter relatively more for small forcing and relatively less for strong forcing.

For the whole AIS and in the perspective of modelled multi-metre GMSL rise contribution, the present-day imbalance has an impact on the AIS mass loss before 2100. All simulations starting from the transient initializations show more integrated mass loss over the AIS in 2100 compared to the simulations starting from the equilibrium initialization, with in most cases a doubled GMSL rise contribution when using the present-day observed mass change rates, except for the simulations forced by HADGEM_RCP585 when considering the ASE region. This forcing contains early ocean warming and little increases in the SMB in the beginning of the simulation, overshadowing almost immediately the differences caused by the transient and equilibrium initialization with a much larger signal. However, simulations forced by both UKESM forcing datasets show the largest and fastest increase in sea level rise over the whole AIS.

After 2150, the emission scenario has the largest impact on the projected mass loss. For the high-end and low-end scenarios, the projected GMSL rise is 1 – 6 and 1 – 2 m, respectively. The difference in projected ocean changes by various ESMs is the next largest source of uncertainty, this will be discussed more below. Lastly, the effect of equilibrium or transient initialisations on the projected GMSL rise from the entire AIS is, in a relative sense, much smaller than in regional simulations focussing on the ASE, or on short-term projections of the AIS. In 2500 for the whole AIS, the difference between transient and equilibrium starting runs is about 1-2 % IVAF change. At a regional ASE simulation and before 2500, the difference can be up to 10-20% IVAF, a tenfold difference.

For high-emission scenarios, incorporating the mass change rates even decreases the GMSL rise contribution. This can be explained by the strength of the warming in these scenarios, which leads to the collapse of major ice shelves in both transient

Deleted: 2

Deleted: Future

Deleted: Mass

Deleted: `

Deleted: `

Deleted:

Deleted: diminishes

Deleted:

Deleted: , for

Deleted: ,

Deleted: ,

Deleted: profoundly

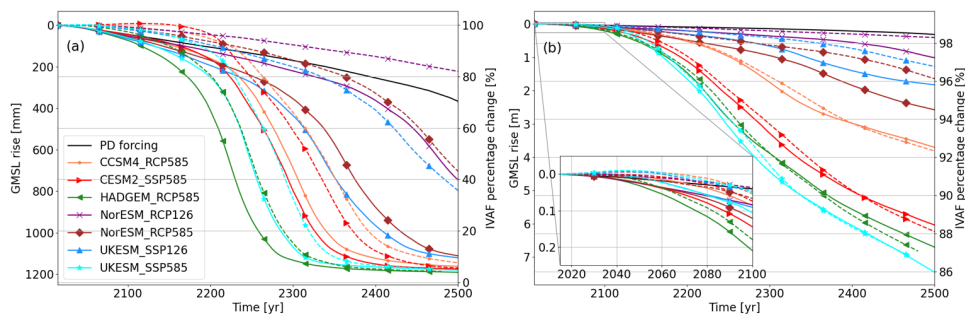
Deleted:

667 and equilibrium initialized simulations. At the same time, observed thickening in parts of the grounded East Antarctic Ice
 668 Sheet (EAIS) continues in the future simulations, offsetting some of the mass loss from West Antarctica. As a result, mass loss
 669 in the WAIS is partially balanced by the increase in thickness in Dronning Maud Land, yielding a similar projected GMSL
 670 rise contribution, see Figure 9. We argue that the spatial distribution of mass change in the transient initialization simulations
 671 is more physically justified compared to the pattern of mass loss in the equilibrium initialization cases, since the former
 672 captures a projected thickening of the EAIS until 2100, in line with recent studies on the forced future of the modelled Antarctic
 673 Ice Sheet (Siahaan et al., 2022; Coulon et al., 2024; Klose et al., 2024; O'Neill et al., 2025) and in line with present-day
 674 observations (Smith et al., 2020).

675

676 The simulations forced with NorESM output (RCP126 and RCP585) show much less mass loss than the others, as both
 677 NorESM simulations have less warming and more enhanced accumulation than the other ESM runs. The NorESM output
 678 assumes a constant climate after 2100, while output from the other ESMs assumes ongoing warming through 2300.

679



680

681 **Figure 9.** Integrated mass loss in the ASE, where Thwaites Glacier and Pine Island Glacier are situated (a). Left y-axis shows the GMSL
 682 rise in mm and right y-axis the Ice Volume Above Floatation in percentage of the initial value. The same for the whole AIS (b). Solid lines
 683 indicate simulations starting with the observed mass change rates, dashed lines indicate simulations starting from an equilibrium. Colors
 684 indicate the ocean forcing scenario used. The black line indicates an unforced transient initialization simulation. PD-forcing denotes a
 685 simulation without any additional ESM forcing, similar to what was done by Van Den Akker et al. (2025b)

686

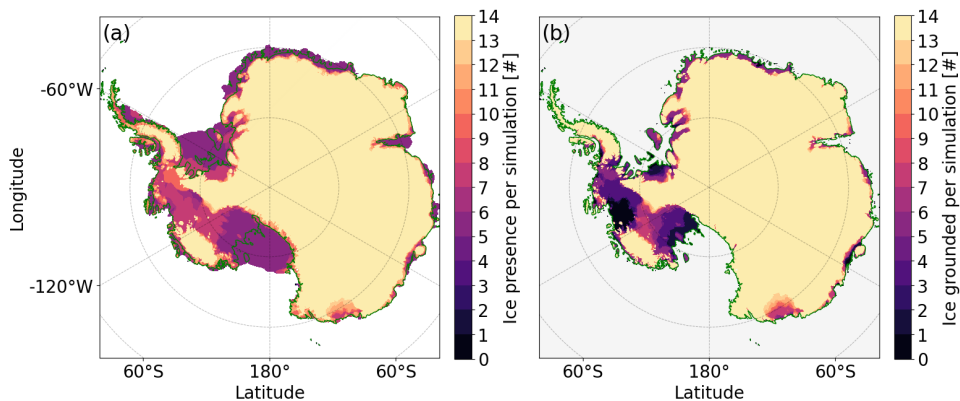
687 Next, we discuss the modelled patterns of ice shelf and grounding line retreat. Figure 10 shows the number of simulations
 688 containing ice (Fig. 10a) and grounded ice (Fig. 10b) across Antarctica for the year 2500. The most significant reduction in
 689 grounded ice area occurs in the WAIS. Aside from Wilkes Land, the grounding line retreat is limited in the EAIS as for most
 690 of the coastline, the inland bedrock is close to or above sea level. All simulations predict substantial grounded ice loss in

691 Thwaites Glacier, as already clear from Figure 6a. While not all scenarios result in a full WAIS collapse, several high-emission
692 scenarios show complete loss of floating ice at the current locations of PIG and TG.

693

694 For half the simulations, the Filchner-Ronne shelf and the Bungenstock Ice Rise (near the southern margin of the Ronne ice
695 shelf) have respectively disappeared and completely ungrounded by 2500. More than half (9 out of 14) simulations end with
696 the Ross shelf completely melted, in some cases along with glaciers at the Siple coast. As our simulations do not model calving
697 for retreated ice shelves, this disintegration is entirely due to enhanced basal melting by warmer ocean waters. In fact, in
698 simulations where the Filchner-Ronne or the Ross shelves effectively disintegrate, the Bungenstock Ice Rise or the Siple Coast
699 also deglaciates, showing a direct relation between the large floating ice shelves and their upstream tributary glaciers.

700



701

702 **Figure 10.** Ice present (a) and grounded (b) at the end (2500) of every simulation per grid cell, summed over all 14 simulations: with 7 ESM
703 scenarios and the 'transient and equilibrium initialization.

704

705 This clear connection between floating and grounded ice mass is further assessed in Figure 11. The floating ice mass and
706 percent change of IVAF since 2015 are shown per region (Filchner-Ronne, Ross and ASE as delineated in Fig. S3) in this
707 figure. Both the Filchner-Ronne and Ross shelves display similar trends. Some ESM forcings result in little change in modelled
708 floating ice mass on the shelves during the simulation. For the Ross shelf, this occurs under UKESM-SSP126 and
709 NorESM_RCP26, while for Filchner-Ronne the same applies with the addition of NorESM_RCP85. In all other scenarios
710 except NorESM_RCP85 for Ross, the volume of floating ice diminishes. This pattern is irrespective of the transient or
711 equilibrium initialization: the dashed and solid lines in Figure 11 show little difference. These regions are currently relatively

Deleted:

Deleted: Southern

Deleted: Even more

715 stable compared to the ASE (Smith et al., 2020). As a result, incorporating the small observed mass change rates in those
716 regions does not affect the mass loss in future projections.

717
718 The loss of floating ice mass is closely tied to the average thermal forcing in each region, as shown in Figure 11. For the
719 Filchner-Ronne shelf, the percent change in IVAF, the floating ice mass loss and the average thermal forcing all follow a
720 consistent pattern. Some ESMs simulate increased thermal forcing at the [F-R](#) calving front, which leads to near-complete shelf
721 collapse and substantial ice mass loss. Others maintain thermal forcing near present-day levels, resulting in a largely intact ice
722 shelf and minimal mass loss. A similar pattern is observed for the Ross shelf, the middle column in Figure 11. The notable
723 exception is NorESM_RCP85, which leads to a reduced Ross shelf in 2300 but not to a complete loss. In this simulation,
724 thermal forcing rises sharply between 2050 and 2100 before stabilizing, which results from repeated climate forcing applied
725 to the NorESM simulations. The early spike is enough to halve the shelf volume quickly, [and](#) the subsequent stabilization
726 allows the remaining half to persist.

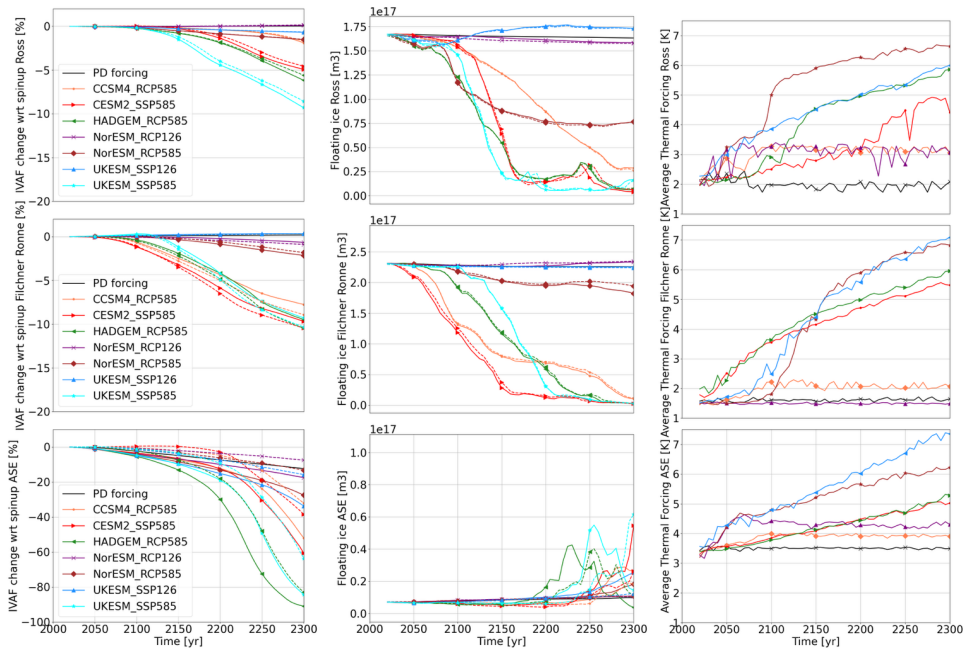
727
728 The ASE region exhibits a distinct pattern. At the beginning of each simulation, there is little floating ice present in the PIG
729 and TG basins. The present-day shelves are small compared to [F-R](#) and Ross. As soon as the grounding line starts to retreat
730 and the grounding line flux increases, a large shelf [forms](#). However, if the thermal forcing is strong enough, this newly formed
731 shelf rapidly melts, producing the increasing and then decreasing pattern of floating ice mass loss in the bottom row of Figure
732 11. Van Den Akker et al. (2025a) provide a more detailed discussion of the role of the shelves on the future dynamics of TG.

733

Deleted: FR

Deleted: FR

Deleted: is formed



737
 738 **Figure 11. Ice volume above floatation (IVAF), floating ice mass and average thermal forcing for Ross (upper row),**
 739 **Filchner Ronne (middle row) and ASE (bottom row) per basin until 2300.** The left column shows the IVAF as a percentage
 740 of what was present at the initialization; the middle column shows the total mass of floating ice per region; the right column
 741 [show](#) the average thermal forcing at 510 m below sea level at the calving front.
 742

743 The loss of grounded ice mass and the reduction in floating ice volume are similarly related for the Ross and Filchner-Ronne
 744 basins. Once a critical fraction of floating ice is lost, the buttressing declines, leading to accelerated upstream flow of grounded
 745 ice, contributing to GMSL rise. To estimate this time lag between the onset of floating ice mass reduction and grounded ice
 746 loss, we calculated the time delay between 10% floating ice mass loss of an ice shelf sector and 5% grounded ice mass loss
 747 from that sector for each simulation and for the Filchner-Ronne and Ross sectors. We excluded the ASE from this analysis as
 748 in this region buttressing has currently little impact on the ice dynamics (Favier et al., 2014; Robel et al., 2019; Lipscomb et
 749 al., 2021; Gudmundsson et al., 2023; Van Den Akker et al., 2025b). Typically, the delay between losing 10% of floating ice
 750 and [losing 5% of grounded ice](#), is [on](#) the order of decades (Table 4). In general, glaciers feeding into the Filchner-Ronne [ice](#)
 751 [shelf](#) respond slightly more rapidly than those along the Siple Coast, indicating that the Filchner-Ronne shelf provides [more](#)

Deleted:

Deleted:

Deleted: %

Deleted: loss

Deleted: in

Deleted: Ice Shelf

Deleted: a little

759 buttressing. Therefore, once 10% of the Filchner-Ronne’s floating ice volume is lost compared to present-day levels, most
 760 simulations show that 5% of grounded ice mass loss (58.7 cm GMSL rise) will follow.

761
 762 Except for NorESM_RCP85, the delay in deglaciation of the FRIS is higher when doing a transient initialization compared to
 763 simulations starting from the equilibrium simulation, while the delay for Ross is often shorter. This is due to an opposite pattern
 764 in the mass change rates of Smith et al. (2020). The Filchner-Ronne shelf is currently thinning, but the grounded ice upstream
 765 is slowly thickening. This is reversed at the Siple Coast and the Ross ice shelf: here the shelf is thickening and the grounded
 766 ice mainly thinning. Adding the mass change rates as was done for the transient initialization makes the grounded ice upstream
 767 of the Filchner-Ronne shelf slightly more stable and at the Siple Coast slightly less stable, and therefore slightly more sensitive
 768 to floating ice mass loss.

769
 770 Significant floating ice volume loss leads in most cases within a century to significant grounded ice loss and sea level rise.
 771 This can be explained by two mechanisms: the sensitivity of the basal melt parameterization to changes in the ocean
 772 temperatures (e.g. the sum of TF_{base} and δT in Eq. (1.5)) and the location of large SMB anomalies. Regarding the former,
 773 when deriving Eq. (1.6) with respect to the sum of TF_{base} and δT and filling in parameter values, we find that the basal melt
 774 parameterization has a temperature change sensitivity of $\sim 11 \text{ m yr}^{-1} \text{ K}^{-1}$ when the sum of TF_{base} and δT is 1 K, increasing
 775 linearly (e.g., when the sum is 2 K, the melt sensitivity is $22 \text{ m yr}^{-1} \text{ K}^{-1}$). For some scenarios, the ocean forcing applied can be
 776 several degrees K, causing an increase in basal melt of hundreds of metres per year, while the SMB anomalies range only from
 777 -2 to 2 m yr^{-1} .

778
 779
 780
 781
 782 **Table 4. Delay in years between a floating ice mass loss of 10% and an IVAF loss of 5% (5% translates to 58.7 cm**
 783 **GMSL rise from FRIS and 24.4 cm from Ross).** The symbol ‘x’ denotes simulations [in which](#) the 10% ice volume above
 784 floatation threshold and/or the 100 mm SLR contribution is never reached. The Filchner-Ronne shelf is abbreviated with
 785 ‘FRIS’, the Ross shelf with ‘Ross’.

ESM forcing	Transient initialization		Equilibrium initialization	
	delay (yr)		delay (yr)	
	FRIS	Ross	FRIS	Ross
CCSM4_RCP85	145	280	130	305
CESM2_SSP585	130	195	120	210

Deleted: when

Split Cells

Formatted Table

HADGEM_RCP85	120	200	110	210
NorESM_RCP26	x	x	x	x
NorESM_RCP85	320	x	x	x
UKESM_SSP126	x	x	x	x
UKESM_SSP585	100	120	80	120

789

790

791 Finally, in Figure 12, we investigate whether the present-day imbalance adds linearly to future climate forcing, by subtracting
792 the no-forcing experiment from all forced experiments. Compared to Figure 7, the differences between the transient and
793 equilibrium simulations are much less pronounced, hence the long-term impact of the current imbalance and future warming
794 looks to add largely linearly. Only when the transiently initialized simulation is in the collapse phase of TG and PIG, the ESM
795 forcing causes a non-linear enhancement of the GMSL rise contribution from the ASE sector (Fig. 12a). This is caused by
796 enhanced ocean warming in the ASE sector compared to the initializations, which is most pronounced in the
797 HADGEM_RCP85 scenarios. The other simulations shown in Fig. 12 that show a distinct difference in response between the
798 equilibrium and transient simulations are UKESM_SSP585 and CESM2_SSP585, both of which include severe drops in the
799 surface mass balance over the grounding line are of the ASE sector (see Fig 2.). All other ESM forcing datasets contain a
800 smaller difference in ocean temperature with the spin-up (see Fig. 1), as well as smaller SMB anomalies, and therefore show
801 a less pronounced difference with their respective control scenario.

802

803 Prior to the collapse phase, the simulations align much more closely than in Figure 7. This may be explained by the fact that,
804 as the TG and PIG basins approach collapse, their mass loss becomes increasingly governed by ice dynamics and less by
805 external forcings. Consequently, simulations starting from equilibrium conditions are more sensitive to gradual warming,
806 which corresponds to the faster increase in GMSL contribution observed in the transiently initialized simulations (Fig. 11,
807 bottom row). As in Figure 7a, the influence of the ESM forcing ceases after the collapse, since WAIS also collapses in the
808 transient simulation without forcing, and WAIS can only collapse once. Lastly, the difference between the transiently and
809 equilibrium-initialized simulations is minimal for the AIS as a whole (Fig. 12b), as the substantial projected GMSL
810 contribution by 2500 from AIS primarily originates from regions outside the ASE sector, which currently remain in balance
811 (Fig. 11).

812

Deleted: if

Deleted: up

Deleted:

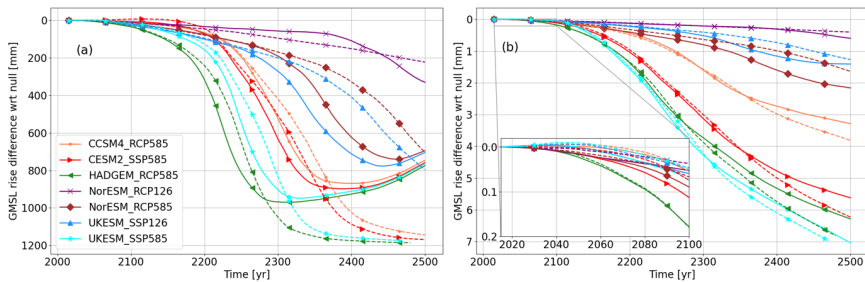
Deleted: up

Deleted: enhancement

Deleted: spinup

Deleted: .).

Deleted: demonstrating that



821
822 **Figure 12. Induced mass loss by the ESM forcings with respect to the unforced simulations, for (a) the ASE and (b) the AIS in terms**
823 **of GMSL rise. Solid lines indicate simulations starting with transient initialization, dashed lines indicate simulations starting from the**
824 **equilibrium [initialization](#). Colors indicate the ocean forcing scenario used.**

Deleted: initialisation.

827 4. Discussion

828 In this study, we show that including the observed present-day mass change rates in an ice sheet model (CISM) improves the
829 quality of projected ice mass loss for the coming century (up until 2100), because it is consistent with the currently observed
830 GMSL rise contribution. Before 2100, including the present-day mass change rates [leads](#) to considerably higher GMSL rise
831 contributions from the AIS, regardless of the ESM forcing chosen. After 2100, dynamic effects like a TG and PIG collapse
832 start to develop, leading to accelerating mass loss. Including the present-day mass change rates accelerates a modelled WAIS
833 collapse by 25 to 100 years in forced simulations. In 2500 for the whole AIS, the difference between transient and equilibrium
834 starting runs is about 1-2 % IVAF change. In regional ASE simulations and before 2500, the difference can be up to 10-20%
835 IVAF, a tenfold difference.

Deleted:

Deleted: lead

837 At the start of our simulations, we find a sea level rise rate of 0.1 – 0.5 mm per year when using the transient initialization
838 method. This is in line with the observed rates reported by Cronin (2012); Smith et al. (2020); Fox-Kemper et al. (2021). In
839 2100, our spread in projected sea level rise from the WAIS and AIS is about 5 – 25 mm, comparable to the present-day
840 observed rate (approximately 0.3 mm yr⁻¹) and in line with Van De Wal et al. (2022). This range is similar to values reported
841 by Edwards et al. (2021); Coulon et al. (2024); Klose et al. (2024); Seroussi et al. (2023); O’neill et al. (2025). In our ensemble,
842 we do not find any cases where the AIS gains net mass during our simulated period, contrasting [with the results of](#) Siahhaan et
843 al. (2022). They found increased snowfall to dominate over increased basal melting, which leads to a net mass gain until 2100,
844 with higher mass gains with warmer climates. However, in simulations done with low climate forcing, they found a steady
845 decrease of ice mass at the WAIS, similar to the results presented in this study. When continued, this could in their simulation

Deleted: ,

Deleted: in the order

Deleted: ,

Deleted: is

Deleted: found by

854 lead to the Marine Ice Sheet Instability and further enhanced mass loss beyond 2100, possibly outpacing mass gain through
855 increased snowfall.

856

857 In 2300, our modelled ensemble shows a GMSL rise contribution of roughly 100 – 1200 mm from the ASE and 100 – 4500
858 mm for the entire Antarctic ice sheet. This large range is linked to dynamic instabilities caused by ice sheet thinning earlier in
859 the simulation. Our ensemble almost captures the range reported by Seroussi et al. (2024); Greve et al. (2023); Payne et al.
860 (2021), with the exception of the cases where the AIS is growing (i.e., when a negative GMSL rise contribution is simulated).
861 The dynamic instability leading to the WAIS collapse is featured in all our simulations, causing large mass losses and thereby
862 compensating any (small) mass gains on the EAIS. Furthermore, the ESM forcing used shows predominantly warming ocean
863 waters and a decreasing SMB over the whole AIS from present-day until 2300 with time, in contrast to Siahhaan et al. (2022),
864 in whose simulations to 2100 the SMB increase dominates over ice dynamical processes.

865

866 Our schematic experiments show that simulations initialized with present-day mass change rates respond less strongly to
867 uniform ocean warming than those using equilibrium initializations. As expected, greater ocean warming triggers an earlier
868 collapse of TG and, subsequently, the ASE basin but with diminishing returns: the most significant impact of additional
869 warming is seen in the low-warming scenarios. Notably, the onset of collapse does not occur before 2100, even with 2 degrees
870 of ocean warming. This is in agreement with earlier WAIS collapse studies: Joughin et al. (2014) mention from 2200 onward,
871 Robel et al. (2019) and Van Den Akker et al. (2025b) mention approximately 500 years onward. This suggests a potential ice
872 dynamical threshold that delays the TG collapse. However, the peak rate of GMSL rise during the collapse continues to increase
873 linearly with additional ocean warming. This aligns with the contrasting patterns in Figures 7 and 12: while the nonlinear
874 enhancement of mass loss by additional ocean warming and present-day mass losses prior to the collapse of the ASE sector is
875 very apparent in the idealized simulations, it is largely absent in the simulations forced with ESM data. Hence, we find that
876 including the present-day mass loss rates increases the modelled GSML from the AIS mainly in the short term when mass loss
877 is dominated by the ASE.

878

879 The relative unimportance of the SMB changes is related to the location of their anomalies. The largest anomalies are found
880 near the coast of the AIS, where in many locations floating ice, or as the simulations progress, no ice at all exists. Therefore,
881 the increased/decreased SMB is not contributing significantly to changes in projected GMSL rise from simulations forced by
882 output from different ESMs. However, the SMB in the CMIP5 and CMIP6 models is determined using the present-day
883 geometry of the Antarctic Ice Sheet. In our simulations, the ice sheet geometry changes drastically, with surface heights
884 decreasing for most of the WAIS. Lower surfaces, through the lapse rate, will yield higher air temperatures and a more negative
885 SMB, which could enhance mass loss more when this effect is incorporated. Ideally, ice sheet modellers should use coupled
886 simulations where atmospheric models directly resolve the SMB of ice sheets based on their evolving geometries. This is
887 computationally expensive and only done for the AIS in recent UKESM studies, such as Siahhaan et al. (2022). Alternatively,

Deleted: WAIS

Deleted: caused by

Deleted: till

Deleted: schematic and

Deleted: ,

Deleted: non-linear

Deleted: are

Deleted: will

Deleted: shown by

897 simple parameterizations of this effect could be used (e.g. Fortuin and Oerlemans (1990)). A solution could be to use SMB
898 emulators, but these have yet to be developed.

899

900 In many simulations shown in our study, all floating ice disappears from the Filchner-Ronne and Ross shelves. This is not
901 uncommon in forced AIS simulations (Coulon et al., 2024; Seroussi, 2021; Seroussi et al., 2024). However, the disappearance
902 of the big ice shelves is controlled by the amount of warming available in their cavities. CISM does not contain a submodule
903 to simulate the overturning circulation in the ice shelf cavities, and neither did the ESMs from which the forcing was used in
904 this study. The thermal forcing was only available in the open ocean bounded by the (observed) calving front of the AIS, and
905 had to be extrapolated into the cavities. Therefore, it cannot be ruled out that the warming simulated in the cavities that lead
906 to dramatic floating ice loss of the large ice shelves is caused (at least in part) by the extrapolation scheme. In essence, the
907 extrapolation scheme now determines when the ice shelf cavities shift from a cold state, which they in are at present, to a warm
908 state. Future studies could improve this aspect by using cavity-resolving ocean models (Scott et al., 2023), or an intermediate
909 complexity 2D layer resolving model like LADDIE (Lambert et al., 2022).

910

911

912 We employed seven forcing datasets derived from five ESMs. Although forcing data were available only to the year 2300, our
913 simulations extended to 2500. To enable CISM to run through 2500, we held the forcing fields (from 2300) constant over the
914 years 2300–2500. This approach could introduce biases if conditions in 2300 differ substantially from those in the surrounding
915 decades. To assess this, we compared the 20-year mean (2280–2300) thermal forcing and surface mass balance (SMB)
916 anomalies, shown in Figs S9 and S10, with the values used for the year 2300 (Figs 1 and 2). For ocean thermal forcing, the
917 year-2300 fields closely match the 20-year mean across all datasets. SMB anomalies show minor differences between the year
918 2300 and the average of 2280-2300, most notably in the NorESM_RCP26 dataset over the Weddell Sea, but overall, the spatial
919 patterns and magnitudes remain highly similar. These comparisons suggest that substituting the 20-year mean for the single
920 year 2300 would not affect our results significantly.

921

922

923 We applied a no-advance calving approach: the calving front was restricted from advancing beyond its present-day observed
924 position. While it was allowed to retreat, primarily due to significant increases in basal melt rates observed in most simulations,
925 calving ceased entirely once the front retreated upstream of its current position. Although this is a conservative and somewhat
926 unphysical representation, it serves as a simplified framework. Incorporating a more physically grounded calving law,
927 accounting for factors such as stress and strain rates, rather than relying solely on modelled ice thickness, could improve
928 predictions of ice mass loss. Integrating such advanced calving schemes into CISM is an area of active research.

929

Deleted: cavity

Deleted: cavity

Deleted: ¶

Deleted: ¶

Deleted: In this study, we

Deleted:

Deleted: up

Deleted: final available

Deleted: considerably

Deleted: modeled

940 **5. Conclusion**

941 In this paper, we show ocean-forced Antarctic-wide simulations conducted with the Community Ice Sheet Model until 2500.
942 We test a new feature of the model: initializing with the present-day observed mass change rates. Schematic ocean warming
943 causes a faster onset of TG collapse with diminishing returns but linearly increasing GMSL rise rates with additional warming.
944 We furthermore find that including the present-day imbalance is important for regional WAIS simulations, where including
945 the present-day mass change rates in a simulation speeds up Thwaites Glacier and Pine Island Glacier collapse by 25 – 100
946 years. Including the mass change rates doubles the AIS GMSL contribution in 2100 in our ensemble. For long-term continental
947 AIS simulations beyond 2100, the choice of the ESM used is more important than the choice to include or not the present-day
948 mass change rates in a century-timescale simulation. We find for all simulations that the AIS will continue to lose mass over
949 the next five centuries, with uncertainties increasing strongly over time.

950
951 Our study highlights that, for simulations until 2500, the main ice losses happen in the Ross and Filchner-Ronne, preceded by
952 mass loss in the ASE region, but the pattern is highly dependent on the extrapolation scheme of ocean properties into the ice
953 shelf cavities. The mass balance of the floating ice shelves proves to be crucial for the grounded ice loss rate. Our simulations
954 do not use a physically based calving scheme or a sub-shelf cavity-resolving ocean model. Replacing both processes with
955 physically based parameterizations or sub-models will likely change the mass balance of the floating shelves and ultimately
956 increase our confidence in sea level rise projections from the Antarctic Ice Sheet. Including a more physically based rather
957 than a location-based calving flux will probably increase the modelled future mass loss of the AIS, and therefore project faster
958 ice sheet retreat and as a consequence, more GMSL rise.

960 **Code availability**

961 CISM is an open-source code developed on the Earth System Community Model Portal (EPSCOMB) Git repository available
962 at <https://github.com/ESCOMP/CISM>. The specific version used to run these experiments will be tagged before publication.

964 **Data availability**

965 The output of the simulations shown in this study will be uploaded to a Zenodo repository before publication.

967 **Author contributions**

968 Tvda designed and executed the main experiments. WHL and GRL developed CISM and helped configure the model for the
969 experiments. RSWvdW, WJvdB, WHL, GRL provided guidance and feedback. Tvda prepared the manuscript, with
970 contributions from all authors.

971
972 Tvda received funding from the NPP programme of NWO. WHL and GRL were supported by the NSF National Center for
973 Atmospheric Research, which is a major facility sponsored by the National Science Foundation (NSF) under Cooperative

Deleted:

Deleted:

Deleted:

Deleted: In our

Deleted: we

Deleted: employ

Deleted:

Deleted:

982 Agreement no. 1852977. Computing and data storage resources for CISM simulations, including the Derecho supercomputer
 983 (<https://doi.org/10.5065/D6RX99HX>), were provided by the Computational and Information Systems Laboratory (CISL) at
 984 NSF NCAR. GRL received additional support from NSF grant no. 2045075.
 985
 986 The authors declare no competing interests.
 987

988 References

989 Adusumilli, S., Fricker, H. A., Medley, B., Padman, L., and Siegfried, M. R.: Interannual variations in meltwater input to the
 990 Southern Ocean from Antarctic ice shelves, *Nature Geoscience*, 13, 616–620, <https://doi.org/10.1038/s41561-020-0616-z>,
 991 2020.
 992 Amaral, T., Bartholomäus, T. C., and Enderlin, E. M.: Evaluation of iceberg calving models against observations from
 993 Greenland outlet glaciers, *Journal of Geophysical Research: Earth Surface*, 125, e2019JF005444,
 994 <https://doi.org/10.1029/2019JF005444>, 2020.
 995 Aschwanden, A., Aðalgeirsdóttir, G., and Khroulev, C.: Hindcasting to measure ice sheet model sensitivity to initial states,
 996 *The Cryosphere*, 7, 1083–1093, <https://doi.org/10.5194/tc-7-1083-2013>, 2013.
 997 Aschwanden, A., Bartholomäus, T. C., Brinkerhoff, D. J., and Truffer, M.: Brief communication: A roadmap towards credible
 998 projections of ice sheet contribution to sea level, *The Cryosphere*, 15, 5705–5715, <https://doi.org/10.5194/tc-15-5705-2021>,
 999 2021.
 1000 Barthel, A., Agosta, C., Little, C. M., Hattermann, T., Jourdain, N. C., Goelzer, H., Nowicki, S., Seroussi, H., Straneo, F., and
 1001 Bracegirdle, T. J.: CMIP5 model selection for ISMIP6 ice sheet model forcing: Greenland and Antarctica, *The Cryosphere*,
 1002 14, 855–879, <https://doi.org/10.5194/tc-14-855-2020>, 2020.
 1003 Beckmann, A. and Goosse, H.: A parameterization of ice shelf–ocean interaction for climate models, *Ocean Modelling*, 5,
 1004 157–170, [https://doi.org/10.1016/S1463-5003\(02\)00035-X](https://doi.org/10.1016/S1463-5003(02)00035-X), 2003.
 1005 Berdahl, M., Leguy, G., Lipscomb, W. H., Urban, N. M., and Hoffman, M. J.: Exploring ice sheet model sensitivity to ocean
 1006 thermal forcing and basal sliding using the Community Ice Sheet Model (CISM), *The Cryosphere*, 17, 1513–1543,
 1007 <https://doi.org/10.5194/tc-17-1513-2023>, 2023.
 1008 Berends, C. J., Goelzer, H., and Van De Wal, R. S.: The Utrecht finite volume ice-sheet model: UFEMISM (version 1.0),
 1009 *Geoscientific Model Development*, 14, 2443–2470, <https://doi.org/10.5194/gmd-14-2443-2021>, 2021.
 1010 Berends, C. J., Goelzer, H., Reerink, T. J., Stap, L. B., and Van De Wal, R. S.: Benchmarking the vertically integrated ice-
 1011 sheet model IMAU-ICE (version 2.0), *Geoscientific Model Development*, 15, 5667–5688, <https://doi.org/10.5194/gmd-15-5667-2022>, 2022.
 1012 Bett, D. T., Bradley, A. T., Williams, C. R., Holland, P. R., Arthern, R. J., and Goldberg, D. N.: Coupled ice/ocean interactions
 1013 during the future retreat of West Antarctic ice streams, *The Cryosphere*, 18, 2653–2675, <https://doi.org/10.5194/tc-18-2653-2024>, 2024.
 1014 Bradley, A. and Arthern, R.: WAVI. jl: A Fast, Flexible, and Friendly Modular Ice Sheet Model, Written in Julia, AGU Fall
 1015 Meeting Abstracts, 2021.
 1016 Choi, Y., Morlighem, M., Wood, M., and Bondzio, J. H.: Comparison of four calving laws to model Greenland outlet glaciers,
 1017 *The Cryosphere*, 12, 3735–3746, <https://doi.org/10.5194/tc-2018-132>, 2018.
 1018 Coulon, V., Klose, A. K., Kittel, C., Edwards, T., Turner, F., Winkelmann, R., and Pattyn, F.: Disentangling the drivers of
 1019 future Antarctic ice loss with a historically calibrated ice-sheet model, *The Cryosphere*, 18, 653–681,
 1020 <https://doi.org/10.5194/tc-18-653-2024>, 2024.
 1021 Cronin, T. M.: Rapid sea-level rise, *Quaternary Science Reviews*, 56, 11–30, <https://doi.org/10.1016/j.quascirev.2012.09.021>,
 1022 2012.
 1023
 1024

Deleted: geoscience

Deleted: -

Deleted: →

Deleted: 2020. →

Deleted: -

Deleted: →

Deleted: -

Deleted: →

Deleted: -

Deleted: →

Deleted: modelling

Deleted: -

Deleted: →

Deleted: -

Deleted: →

Deleted: -

Deleted: →

Deleted: -

Deleted: →

Deleted: Discussions, 2023, 1-28, 2023. →

Deleted: C11A-03, →

Deleted: -

Deleted: →

Deleted: -

Deleted: →

Deleted: -

Deleted: →

1052 Danabasoglu, G., Lamarque, J. F., Bacmeister, J., Bailey, D., DuVivier, A., Edwards, J., Emmons, L., Fasullo, J., Garcia, R.,
1053 and Gettelman, A.: The community earth system model version 2 (CESM2), *Journal of Advances in Modeling Earth Systems*,
1054 12, e2019MS001916, <https://doi.org/10.1029/2019MS001916>, 2020.

1055 DeConto, R. M., Pollard, D., Alley, R. B., Velicogna, I., Gasson, E., Gomez, N., Sadai, S., Condrón, A., Gilford, D. M., and
1056 Ashe, E. L.: The Paris Climate Agreement and future sea-level rise from Antarctica, *Nature*, 593, 83–89,
1057 <https://doi.org/10.1038/s41586-021-03427-0>, 2021.

1058 Edwards, T. L., Nowicki, S., Marzeion, B., Hock, R., Goelzer, H., Seroussi, H., Jourdain, N. C., Slater, D. A., Turner, F. E.,
1059 and Smith, C. J.: Projected land ice contributions to twenty-first-century sea level rise, *Nature*, 593, 74–82,
1060 <https://doi.org/10.1038/s41586-021-03302-y>, 2021.

1061 Favier, L., Jourdain, N. C., Jenkins, A., Merino, N., Durand, G., Gagliardini, O., Gillet-Chaulet, F., and Mathiot, P.:
1062 Assessment of sub-shelf melting parameterisations using the ocean–ice-sheet coupled model NEMO (v3.6)–Elmer/Ice (v8.3),
1063 *Geoscientific Model Development*, 12, 2255–2283, <https://doi.org/10.5194/gmd-12-2255-2019>, 2019.

1064 Favier, L., Durand, G., Cornford, S. L., Gudmundsson, G. H., Gagliardini, O., Gillet-Chaulet, F., Zwinger, T., Payne, A., and
1065 Le Brocq, A. M.: Retreat of Pine Island Glacier controlled by marine ice-sheet instability, *Nature Climate Change*, 4, 117–
1066 121, <https://doi.org/10.1038/nclimate2094>, 2014.

1067 Fortuin, J. and Oerlemans, J.: Parameterization of the annual surface temperature and mass balance of Antarctica, *Annals of*
1068 *Glaciology*, 14, 78–84, 1990.

1069 Fox-Kemper, B., Hewitt, H. T., C., Aðalgeirsdóttir, G., Drijfhout, S. S., Edwards, T. L., Golledge, N. R., Hemer, M., Kopp,
1070 R. E., Krinner, G., Mix, A., Notz, D., Nowicki, S., Nurhati, I. S., Ruiz, L., Sallée, J.-B., Slangen, A. B. A., and Yu, Y.: Ocean,
1071 Cryosphere and Sea Level Change, in *Climate Change 2021: The Physical Science Basis*, Cambridge University Press, 1211–
1072 1362, <https://doi.org/10.1017/9781009157896.011>, 2021.

1073 Goldberg, D. N.: A variationally derived, depth-integrated approximation to a higher-order glaciological flow model, *Journal*
1074 *of Glaciology*, 57, 157–170, <https://doi.org/10.3189/002214311795306763>, 2011.

1075 Greene, C. A., Gardner, A. S., Schlegel, N.-J., and Fraser, A. D.: Antarctic calving loss rivals ice-shelf thinning, *Nature*, 609,
1076 948–953, <https://doi.org/10.1038/s41586-022-05037-w>, 2022.

1077 Greve, R. and Blatter, H.: Comparison of thermodynamics solvers in the polythermal ice sheet model SICOPOLIS, *Polar*
1078 *Science*, 10, 11–23, <https://doi.org/10.1016/j.polar.2016.02.002>, 2016.

1079 Greve, R., Chambers, C., Obase, T., Saito, F., Chan, W.-L., and Abe-Ouchi, A.: Future projections for the Antarctic ice sheet
1080 until the year 2300 with a climate-index method, *Journal of Glaciology*, 69, 1569–1579, <https://doi.org/10.1017/jog.2023.41>,
1081 2023.

1082 Gudmundsson, G., Krug, J., Durand, G., Favier, L., and Gagliardini, O.: The stability of grounding lines on retrograde slopes,
1083 *The Cryosphere*, 6, 1497–1505, <https://doi.org/10.5194/tc-6-1497-2012>, 2012.

1084 Gudmundsson, G. H., Barnes, J. M., Goldberg, D., and Morlighem, M.: Limited impact of Thwaites Ice Shelf on future ice
1085 loss from Antarctica, *Geophysical Research Letters*, 50, e2023GL102880, <https://doi.org/10.1029/2023GL102880>, 2023.

1086 Joughin, I., Smith, B. E., and Medley, B.: Marine ice sheet collapse potentially under way for the Thwaites Glacier Basin,
1087 West Antarctica, *Science*, 344, 735–738, <https://doi.org/10.1126/science.1249055>, 2014.

1088 Joughin, I., Smith, B. E., and Schoof, C. G.: Regularized Coulomb friction laws for ice sheet sliding: Application to Pine Island
1089 Glacier, Antarctica, *Geophysical Research Letters*, 46, 4764–4771, <https://doi.org/10.1029/2019GL082526>, 2019.

1090 Jourdain, N. C., Asay-Davis, X., Hattermann, T., Straneo, F., Seroussi, H., Little, C. M., and Nowicki, S.: A protocol for
1091 calculating basal melt rates in the ISMIP6 Antarctic ice sheet projections, *The Cryosphere*, 14, 3111–3134,
1092 <https://doi.org/10.5194/tc-14-3111-2020>, 2020.

1093 Klose, A. K., Coulon, V., Pattyn, F., and Winkelmann, R.: The long-term sea-level commitment from Antarctica, *The*
1094 *Cryosphere*, 18, 4463–4492, <https://doi.org/10.5194/tc-18-4463-2024>, 2024.

1095 Lambert, E., Jüling, A., Van De Wal, R. S., and Holland, P. R.: Modeling Antarctic ice shelf basal melt patterns using the one-
1096 Layer Antarctic model for Dynamical Downscaling of Ice–ocean Exchanges (LADDIE), *The Cryosphere Discussions*, 2022,
1097 1–39, 2022.

1098 Leguy, G., Asay-Davis, X., and Lipscomb, W.: Parameterization of basal friction near grounding lines in a one-dimensional
1099 ice sheet model, *The Cryosphere*, 8, 1239–1259, <https://doi.org/10.5194/tc-8-1239-2014>, 2014.

1100 Leguy, G. R., Lipscomb, W. H., and Asay-Davis, X. S.: Marine ice sheet experiments with the Community Ice Sheet Model,
1101 *The Cryosphere*, 15, 3229–3253, <https://doi.org/10.5194/tc-15-3229-2021>, 2021.

Deleted: 2020. →

Deleted: ...89, <https://doi.org/10.1038/s41586-021-03427-0>, 2021. → ... [1]

Deleted: ...82, <https://doi.org/10.1038/s41586-021-03302-y>, 2021. → ... [2]

Deleted: ...–Elmer/Ice (v8. ...), *Geoscientific Model Development*, 12, 2255–...2283, 2019. → ... [3]

Deleted: ...121, <https://doi.org/10.1038/nclimate2094>, 2014. → ... [4]

Deleted: ...84, 1990. → ... [5]

Deleted: H.T. ...ewitt, H. T., C. X., Aðalgeirsdóttir..., Aðalgeirsdóttir, G., Drijfhout, S. S., Edwards, T. L., Golledge, N. R., Hemer, M., Kopp, R. E., Krinner, G., Mix, A., Notz, D., Nowicki, S., Nurhati, I. S., Ruiz, L., Sallée, J.-B., Slangen, A. B. A., and Yu, Y.: Ocean, Cryosphere and Sea Level Change. In... in *Climate Change 2021: The Physical Science Basis*. Contribution of Working Group I to the Sixth Assessment Report of the Intergovernmental Panel on Climate Change... Cambridge Press, Cambridge, United Kingdom and New York, NY, USA, 1211–...1362, <https://doi.org/10.1017/9781009157896.011>, 2021. → ... [6]

Deleted: ...170, <https://doi.org/10.3189/002214311795306763>, 2011. → ... [7]

Deleted: ...953, <https://doi.org/10.1038/s41586-022-05037-w>, 2022. → ... [8]

Deleted: ...23, <https://doi.org/10.1016/j.polar.2016.02.002>. → ... [9]

Deleted: ...1579, <https://doi.org/10.1017/jog.2023.41>, 2023. → ... [10]

Deleted: ...1505, <https://doi.org/10.5194/tc-6-1497-2012>. → ... [11]

Deleted: 2023. → ... [12]

Deleted: ...738, <https://doi.org/10.1126/science.1249055>. → ... [12]

Deleted: research letters...research Letters, 46, 4764–...4771, <https://doi.org/10.1029/2019GL082526>, 2019. → ... [13]

Deleted: ...3134, <https://doi.org/10.5194/tc-14-3111-2020>. → ... [14]

Deleted: ...4492, <https://doi.org/10.5194/tc-18-4463-2024>. → ... [15]

Deleted: ...39, 2022. → ... [16]

Deleted: ...1259, <https://doi.org/10.5194/tc-8-1239-2014>. → ... [17]

Deleted: -3253, 2021. →

1186 Levermann, A., Albrecht, T., Winkelmann, R., Martin, M., Haseloff, M., and Joughin, I.: Kinematic first-order calving law
1187 implies potential for abrupt ice-shelf retreat, *The Cryosphere*, 6, 273–286, <https://doi.org/10.5194/tc-6-273-2012>, 2012.

1188 Li, L., Aitken, A. R. A., Lindsay, M. D., and Kulessa, B.: Sedimentary basins reduce stability of Antarctic ice streams through
1189 groundwater feedbacks, *Nature Geoscience*, 15, 645–650, <https://doi.org/10.1038/s41561-022-00992-5>, 2022.

1190 Lipscomb, W. H., Leguy, G. R., Jourdain, N. C., Asay-Davis, X., Seroussi, H., and Nowicki, S.: ISMIP6-based projections of
1191 ocean-forced Antarctic Ice Sheet evolution using the Community Ice Sheet Model, *The Cryosphere*, 15, 633–661,
1192 <https://doi.org/10.5194/tc-15-633-2021>, 2021.

1193 Lipscomb, W. H., Price, S. F., Hoffman, M. J., Leguy, G. R., Bennett, A. R., Bradley, S. L., Evans, K. J., Fyke, J. G., Kennedy,
1194 J. H., and Perego, M.: Description and evaluation of the community ice sheet model (CISM) v2.1, *Geoscientific Model*
1195 *Development*, 12, 387–424, <https://doi.org/10.5194/gmd-12-387-2019>, 2019.

1196 Meehl, G. A., Senior, C. A., Eyring, V., Flato, G., Lamarque, J.-F., Stouffer, R. J., Taylor, K. E., and Schlund, M.: Context for
1197 interpreting equilibrium climate sensitivity and transient climate response from the CMIP6 Earth system models, *Science*
1198 *Advances*, 6, eaba1981, <https://doi.org/10.1126/sciadv.aba1981>, 2020.

1199 Morlighem, M., Rignot, E., Seroussi, H., Larour, E., Ben Dhia, H., and Aubry, D.: A mass conservation approach for mapping
1200 glacier ice thickness, *Geophysical Research Letters*, 38, L19503, <https://doi.org/10.1029/2011GL048659>, 2011.

1201 Morlighem, M., Rignot, E., Binder, T., Blankenship, D., Drews, R., Eagles, G., Eisen, O., Ferraccioli, F., Forsberg, R., and
1202 Fretwell, P.: Deep glacial troughs and stabilizing ridges unveiled beneath the margins of the Antarctic ice sheet, *Nature*
1203 *Geoscience*, 13, 132–137, <https://doi.org/10.1038/s41561-019-0510-8>, 2020.

1204 Mottram, R., Hansen, N., Kittel, C., Van Wessum, J. M., Agosta, C., Amory, C., Boberg, F., Van De Berg, W. J., Fettweis, X.,
1205 and Gossart, A.: What is the surface mass balance of Antarctica? An intercomparison of regional climate model estimates, *The*
1206 *Cryosphere*, 15, 3751–3784, <https://doi.org/10.5194/tc-15-3751-2021>, 2021.

1207 Nowicki, S., Payne, A. J., Goelzer, H., Seroussi, H., Lipscomb, W. H., Abe-Ouchi, A., Agosta, C., Alexander, P., Asay-Davis,
1208 X. S., and Barthel, A.: Experimental protocol for sealevel projections from ISMIP6 standalone ice sheet models, *The*
1209 *Cryosphere Discussions*, 2020, 1–40, 2020.

1210 Nowicki, S. M., Payne, A., Larour, E., Seroussi, H., Goelzer, H., Lipscomb, W., Gregory, J., Abe-Ouchi, A., and Shepherd,
1211 A.: Ice sheet model intercomparison project (ISMIP6) contribution to CMIP6, *Geoscientific Model Development*, 9, 4521–
1212 4545, <https://doi.org/10.5194/gmd-9-4521-2016>, 2016.

1213 O'Neill, J. F., Edwards, T. L., Martin, D. F., Shafer, C., Cornford, S. L., Seroussi, H. L., Nowicki, S., Adhikari, M., and
1214 Gregoire, L. J.: ISMIP6-based Antarctic projections to 2100: simulations with the BISICLES ice sheet model, *The Cryosphere*,
1215 19, 541–563, 2025.

1216 Pattyn, F. and Morlighem, M.: The uncertain future of the Antarctic Ice Sheet, *Science*, 367, 1331–1335,
1217 <https://doi.org/10.1126/science.aaz5487>, 2020.

1218 Payne, A. J., Nowicki, S., Abe-Ouchi, A., Agosta, C., Alexander, P., Albrecht, T., Asay-Davis, X., Aschwanden, A., Barthel,
1219 A., and Bracegirdle, T. J.: Future sea level change under coupled model intercomparison project phase 5 and phase 6 scenarios
1220 from the Greenland and Antarctic ice sheets, *Geophysical Research Letters*, 48, e2020GL091741,
1221 <https://doi.org/10.1029/2020GL091741>, 2021.

1222 Pollard, D. and DeConto, R.: Description of a hybrid ice sheet-shelf model, and application to Antarctica, *Geoscientific Model*
1223 *Development*, 5, 1273–1295, <https://doi.org/10.5194/gmd-5-1273-2012>, 2012.

1224 Quiquet, A., Dumas, C., Ritz, C., Peyaud, V., and Roche, D. M.: The GRISLI ice sheet model (version 2.0): calibration and
1225 validation for multi-millennial changes of the Antarctic ice sheet, *Geoscientific Model Development*, 11, 5003–5025,
1226 <https://doi.org/10.5194/gmd-11-5003-2018>, 2018.

1227 Reese, R., Garbe, J., Hill, E. A., Urruty, B., Naughten, K. A., Gagliardini, O., Durand, G., Gillet-Chaulet, F., Gudmundsson,
1228 G. H., and Chandler, D.: The stability of present-day Antarctic grounding lines – Part 2: Onset of irreversible retreat of
1229 Amundsen Sea glaciers under current climate on centennial timescales cannot be excluded, *The Cryosphere*, 17, 3761–3783,
1230 <https://doi.org/10.5194/tc-17-3761-2023>, 2023.

1231 Rignot, E., Mouginot, J., and Scheuchl, B.: Ice flow of the Antarctic ice sheet, *Science*, 333, 1427–1430,
1232 <https://doi.org/10.1126/science.1208336>, 2011.

1233 Rignot, E., Jacobs, S., Mouginot, J., and Scheuchl, B.: Ice-shelf melting around Antarctica, *Science*, 341, 266–270,
1234 <https://doi.org/10.1126/science.1235798>, 2013.

Deleted: -

Deleted: →

Deleted: -

Deleted: →

Deleted: -

Deleted: →

Deleted:

Deleted: -

Deleted: →

Deleted: 2020.→

Deleted: 2011.→

Deleted: -

Deleted: →

Deleted: -

Deleted: →

Deleted: -

Deleted: →

Deleted: model development

Deleted: -

Deleted: →

Deleted: -

Deleted: →

Deleted: -

Deleted: →

Deleted: -

Deleted: 2021.→

Deleted: -

Deleted: →

Deleted: -

Deleted: →

Deleted: -

Deleted: →

Deleted: -

Deleted: →

Deleted: -

1273 Robel, A. A., Seroussi, H., and Roe, G. H.: Marine ice sheet instability amplifies and skews uncertainty in projections of future
1274 sea-level rise, *Proceedings of the National Academy of Sciences*, 116, 14887–14892,
1275 <https://doi.org/10.1073/pnas.1904822116>, 2019.

1276 Robinson, A., Goldberg, D., and Lipscomb, W. H.: A comparison of the stability and performance of depth-integrated ice-
1277 dynamics solvers, *The Cryosphere*, 16, 689–709, <https://doi.org/10.5194/tc-16-689-2022>, 2022.

1278 Rosier, S. H., Gudmundsson, G. H., Jenkins, A., and Naughten, K. A.: Calibrated sea level contribution from the Amundsen
1279 Sea sector, West Antarctica, under RCP8.5 and Paris 2 °C scenarios [preprint], *EGUsphere*, 2024.

1280 Rosier, S. H., Reese, R., Donges, J. F., De Rydt, J., Gudmundsson, G. H., and Winkelmann, R.: The tipping points and early
1281 warning indicators for Pine Island Glacier, West Antarctica, *The Cryosphere*, 15, 1501–1516, <https://doi.org/10.5194/tc-15-1501-2021>, 2021.

1282 Schoof, C.: *The effect of cavitation on glacier sliding*, *Proceedings of the Royal Society A: Mathematical, Physical and*
1283 *Engineering Sciences*, 461, 609–627, <https://doi.org/10.1098/rspa.2004.1350>, 2005.

1284 Scott, W. I., Kramer, S. C., Holland, P. R., Nicholls, K. W., Siegert, M. J., and Piggott, M. D.: Towards a fully unstructured
1285 ocean model for ice shelf cavity environments: Model development and verification using the Firedrake finite element
1286 framework, *Ocean Modelling*, 182, 102178, <https://doi.org/10.1016/j.ocemod.2023.102178>, 2023.

1287 Seroussi, H.: Insights on the vulnerability of Antarctic glaciers from the ISMIP6 ice sheet model ensemble, *AGU Fall Meeting*
1288 *Abstracts*, C15C-0818.

1289 Seroussi, H. and Morlighem, M.: Representation of basal melting at the grounding line in ice flow models, *The Cryosphere*,
1290 12, 3085–3096, <https://doi.org/10.5194/tc-12-3085-2018>, 2018.

1291 Seroussi, H., Nowicki, S., Payne, A. J., Goelzer, H., Lipscomb, W. H., Abe-Ouchi, A., Agosta, C., Albrecht, T., Asay-Davis,
1292 X., and Barthel, A.: ISMIP6 Antarctica: a multi-model ensemble of the Antarctic ice sheet evolution over the 21st century,
1293 *The Cryosphere*, 14, 3033–3070, <https://doi.org/10.5194/tc-14-3033-2020>, 2020.

1294 Seroussi, H., Pelle, T., Lipscomb, W. H., Abe-Ouchi, A., Albrecht, T., Alvarez-Solas, J., Asay-Davis, X., Barre, J. B., Berends,
1295 C. J., and Bernaldes, J.: Evolution of the Antarctic Ice Sheet over the next three centuries from an ISMIP6 model ensemble,
1296 *Earth's Future*, 12, e2024EF004561, <https://doi.org/10.1029/2024EF004561>, 2024.

1297 Seroussi, H., Verjans, V., Nowicki, S., Payne, A. J., Goelzer, H., Lipscomb, W. H., Abe-Ouchi, A., Agosta, C., Albrecht, T.,
1298 and Asay-Davis, X.: Insights on the vulnerability of Antarctic glaciers from the ISMIP6 ice sheet model ensemble and
1299 associated uncertainty, *The Cryosphere Discussions*, 2023, 1–28, 2023.

1300 Siahann, A., Smith, R. S., Holland, P. R., Jenkins, A., Gregory, J. M., Lee, V., Mathiot, P., Payne, A. J., Ridley, J. K., and
1301 Jones, C. G.: The Antarctic contribution to 21st-century sea-level rise predicted by the UK Earth System Model with an
1302 interactive ice sheet, *The Cryosphere*, 16, 4053–4086, <https://doi.org/10.5194/tc-16-4053-2022>, 2022.

1303 Smith, B., Fricker, H. A., Gardner, A. S., Medley, B., Nilsson, J., Paolo, F. S., Holschuh, N., Adusumilli, S., Brunt, K., and
1304 Csatho, B.: Pervasive ice sheet mass loss reflects competing ocean and atmosphere processes, *Science*, 368, 1239–1242,
1305 <https://doi.org/10.1126/science.aaz5845>, 2020.

1306 van Calcar, C., Bernaldes, J., Berends, C., van der Wal, W., and van de Wal, R.: Bedrock uplift reduces Antarctic sea-level
1307 contribution over next centuries, 2024.

1308 van de Wal, R. S., Nicholls, R. J., Behar, D., McInnes, K., Stammer, D., Lowe, J. A., Church, J. A., DeConto, R., Fettweis,
1309 X., and Goelzer, H.: A [high-end estimate of sea level rise for practitioners](#), *Earth's Future*, 10, e2022EF002751,
1310 <https://doi.org/10.1029/2022EF002751>, 2022.

1311 van den Akker, T., Lipscomb, W. H., Leguy, G. R., van de Berg, W. J., and van de Wal, R. S. W.: Competing processes
1312 determine the long-term impact of basal friction parameterizations for Antarctic mass loss, *EGUsphere*, 2025, 1–35,
1313 <https://doi.org/10.5194/egusphere-2025-441>, 2025a.

1314 van den Akker, T., Lipscomb, W. H., Leguy, G. R., Bernaldes, J., Berends, C. J., van de Berg, W. J., and van de Wal, R. S.:
1315 Present-day mass loss rates are a precursor for West Antarctic Ice Sheet collapse, *The Cryosphere*, 19, 283–301, 2025b.

1316 Van Wessem, J. M., Van De Berg, W. J., Noël, B. P., Van Meijgaard, E., Amory, C., Birnbaum, G., Jakobs, C. L., Krüger, K.,
1317 Lenaerts, J. T., and Lhermitte, S.: Modelling the climate and surface mass balance of polar ice sheets using RACMO2–Part 2:
1318 Antarctica (1979–2016), *The Cryosphere*, 12, 1479–1498, <https://doi.org/10.5194/tc-12-1479-2018>, 2018.

1319 Wilner, J. A., Morlighem, M., and Cheng, G.: Evaluation of four calving laws for Antarctic ice shelves, *The Cryosphere*
1320 *Discussions*, 2023, 1–19, 2023.

Deleted: -

Deleted: →

Deleted: -

Deleted: →

Deleted: -

Deleted: 2C

Deleted: →

Deleted: -

Deleted: →

Deleted: 2023, →

Deleted: , →

Deleted: -

Deleted: →

Deleted: -

Deleted: →

Deleted: -

Deleted: -

Deleted: -

Deleted: -

Deleted: Earth's

Deleted: →

Deleted: -

Deleted: -

Deleted: →

Deleted: -

Deleted: -

Deleted: →

Deleted: →

Deleted: High-End Estimate

Deleted: Sea Level Rise

Deleted: Practitioners, Earth's future

Deleted: →

Deleted: -

Deleted: →

Deleted: -

Deleted: →

Deleted: -

Deleted: →

Deleted: -

Deleted: →

1362 Winkelmann, R., Martin, M. A., Haseloff, M., Albrecht, T., Bueller, E., Khroulev, C., and Levermann, A.: The Potsdam parallel
1363 ice sheet model (PISM-PIK)–Part 1: Model description, *The Cryosphere*, 5, 715–726, <https://doi.org/10.5194/tc-5-715-2011>,
1364 [2011](https://doi.org/10.5194/tc-5-715-2011).
1365 Yu, H., Rignot, E., Seroussi, H., Morlighem, M., and Choi, Y.: Impact of iceberg calving on the retreat of Thwaites Glacier,
1366 West Antarctica over the next century with different calving laws and ocean thermal forcing, *Geophysical Research Letters*,
1367 46, 14539–14547, <https://doi.org/10.1029/2019GL084966>, 2019.
1368 Zoet, L. K. and Iverson, N. R.: A slip law for glaciers on deformable beds, *Science*, 368, 76–78,
1369 <https://doi.org/10.1126/science.aaz1183>, 2020.
1370

Deleted: -

Deleted: .->

Deleted: -

Deleted: ->

Deleted: -

Deleted: ->

Deleted: ¶

Page 31: [13] Deleted **Tim van den Akker** **2/6/26 10:06:00 AM**



Page 31: [13] Deleted **Tim van den Akker** **2/6/26 10:06:00 AM**



Page 31: [13] Deleted **Tim van den Akker** **2/6/26 10:06:00 AM**



Page 31: [14] Deleted **Tim van den Akker** **2/6/26 10:06:00 AM**



Page 31: [14] Deleted **Tim van den Akker** **2/6/26 10:06:00 AM**



Page 31: [15] Deleted **Tim van den Akker** **2/6/26 10:06:00 AM**



Page 31: [15] Deleted **Tim van den Akker** **2/6/26 10:06:00 AM**



Page 31: [16] Deleted **Tim van den Akker** **2/6/26 10:06:00 AM**



Page 31: [16] Deleted **Tim van den Akker** **2/6/26 10:06:00 AM**



Page 31: [17] Deleted **Tim van den Akker** **2/6/26 10:06:00 AM**



Page 31: [17] Deleted **Tim van den Akker** **2/6/26 10:06:00 AM**

